Published in final edited form as:

Cell Rep. 2020 August 18; 32(7): 108047. doi:10.1016/j.celrep.2020.108047.

Fractalkine-Dependent Microglial Pruning of Viable Oligodendrocyte Progenitor Cells Regulates Myelination

Ashley D. Nemes-Baran[1], **Donovan R. White**[1], **Tara M. DeSilva**[1,2,*]

[1]Department of Neurosciences, Lerner Research Institute, Cleveland Clinic Foundation, Cleveland, OH, USA

[2]Lead Contact

SUMMARY

Oligodendrogenesis occurs during early postnatal development, coincident with neurogenesis and synaptogenesis, raising the possibility that microglia-dependent pruning mechanisms that modulate neurons regulate myelin sheath formation. Here we show a population of ameboid microglia migrating from the ventricular zone into the *corpus callosum* during early postnatal development, termed “the fountain of microglia,” phagocytosing viable oligodendrocyte progenitor cells (OPCs) before onset of myelination. Fractalkine receptor-deficient mice exhibit a reduction in microglial engulfment of viable OPCs, increased numbers of oligodendrocytes, and reduced myelin thickness but no change in axon number. These data provide evidence that microglia phagocytose OPCs as a homeostatic mechanism for proper myelination. A hallmark of hypomyelinating developmental disorders such as periventricular leukomalacia and of adult demyelinating diseases such as multiple sclerosis is increased numbers of oligodendrocytes but failure to myelinate, suggesting that microglial pruning of OPCs may be impaired in pathological states and hinder myelination.

In Brief

Nemes-Baran et al. show that ameboid microglia engulf living oligodendrocyte progenitor cells (OPCs) during brain development. Fractalkine receptor-deficient microglia exhibit a reduction in engulfment of OPCs, resulting in a surplus of oligodendrocytes and impaired myelination. These data provide evidence that microglia phagocytose OPCs as a homeostatic mechanism required for normal myelination.

Graphical Abstract

*Correspondence: desilvt@ccf.org.

AUTHOR CONTRIBUTIONS

T.M.D. and A.D.N.-B. conceived the study and designed the experiments. A.D.N.-B. completed the engulfment and EM analyses. A.D.N.-B. and D.W. contributed to immunohisochemistry. T.M.D. and A.D.N.-B. drafted the manuscript and D.R.W. was involved in editing and discussions.

DECLARATION OF INTERESTS

The authors declare no competing interests.

SUPPLEMENTAL INFORMATION

Supplemental Information can be found online at https://doi.org/10.1016/j.celrep.2020.108047.

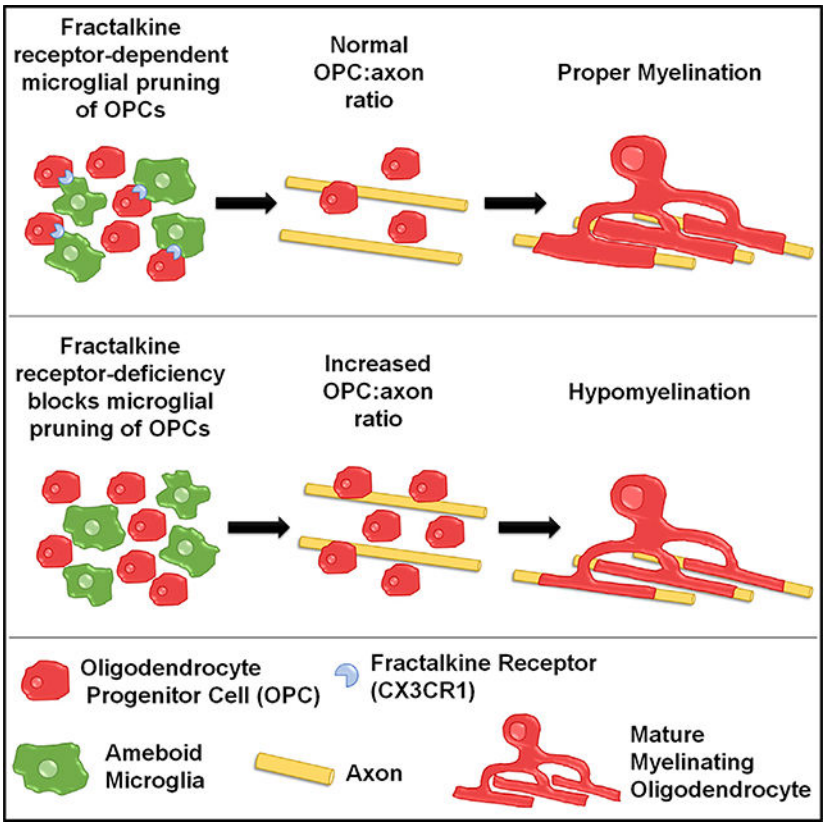

INTRODUCTION

Historically, microglia have been surmised to principally play a role in the neuroinflammatory responses of disease and injury. Recent literature highlights their importance in performing surveillance and neuroprotective functions (Ueno et al., 2013; Vinet et al., 2012; Davalos et al., 2005; Nimmerjahn et al., 2005). Moreover, three different innate immune receptors are expressed on microglia (triggering receptor expressed on myeloid cells 2, complement receptor 3, and fractalkine receptor) regulate synaptic pruning to modulate developmental brain connectivity (Schafer et al., 2012' Filipello et al., 2018; Paolicelli et al., 2011). Furthermore, microglial engulfment of neural precursor cells regulates the developing cerebral cortex (Cunningham et al., 2013), and newborn neurons in the adult dentate gyrus are pruned during neurogenesis (Sierra et al., 2010) to modify synaptic transmission (Adlaf et al., 2017). Oligodendrogenesis (Kessaris et al., 2006; Levison and Goldman, 1993) occurs at an early postnatal time point, coincident with neurogenesis and synaptogenesis, suggesting that microglia-dependent homeostatic mechanisms that regulate neurons may also play an important role in myelin sheath formation, critical for transmission of action potentials (Smith and Koles, 1970) and metabolic support to axons (Lee et al., 2012; Fünfschilling et al., 2012). Interestingly, during this same time period in development, microglia with an ameboid morphology migrate from the ventricular zone into the *corpus callosum*, originally documented as "the fountain of microglia" (Imamoto and Leblond, 1978; Ling, 1979).

RESULTS

3D Confocal Reconstruction Shows the Fountain of Microglia Engulfing OPCs during a Restricted Window of White Matter Development

Using a genetically encoded fluorescent reporter, CX3CR1:GFP, for microglia, green ramified cells were found evenly dispersed throughout the brain on embryonic day 14 (E14) (Figure S1A), as described previously (Ginhoux et al., 2010; Gomez Perdiguero et al., 2015). On E20, a second population of CX3CR1:GFP cells with ameboid morphology emerged from the ventricular zone (Figure S1B) and increased in density on post-natal day 0 (P0) (Figure S2A). This population infiltrated the *corpus callosum* by P3 (Figure S2B), increasing in number on P5 (Figure S2C) and P7 (Figure S2D), forming the fountain of microglia (Imamoto and Leblond, 1978; Ling, 1979). Ameboid microglia are predominantly located within the *corpus callosum* (Figures S1C and S1D). Cortical microglia (Figure S1E) are morphologically distinct from ameboid microglia (Figure S1F) found in the *corpus callosum* during this early postnatal time period. Colocalization with anti-Iba-1 confirmed that this population of ameboid CX3CR1:GFP cells in the *corpus callosum* is of the myeloid lineage (Figures S3A–S3F). To explore the possibility that the fountain of microglia is derived from peripheral circulating monocytes, CCR2:RFP reporter mice crossed with CX3CR1:GFP reporter mice were used. CCR2 (chemokine C-C motif receptor 2) is a member of the beta chemokine receptor family expressed exclusively by peripheral monocytes (Mizutani et al., 2012; Saederup et al., 2010). Confocal imaging of the *corpus callosum* on P4 and P7 showed green CX3CR1-expressing cells but no red CCR2-expressing cells (Figures S3G and S3H), as reported previously (Hagemeyer et al., 2017). The spleen served as a positive internal control.

Ameboid microglia infiltrate the *corpus callosum* during a restricted time period that parallels oligodendrogenesis. To evaluate this potential interaction, NG2:Tom reporter mice were used to fate-map oligodendrocyte progenitor cells (OPCs) in the *corpus callosum*, and microglia were immunostained with Iba-1. Confocal 3D reconstruction was performed in the *corpus callosum* above the lateral ventricles (Figure 1A, white boxes). A high-powered view of a 0.3-μm plane from a z stack shows red OPCs within green microglia at P7 (Figures 1B–1D; Video S1). Representative confocal 3D reconstruction at P4 demonstrates ameboid microglia with bushy processes in contact with OPCs (Figure 1E). At P7, ameboid microglia with few processes are engulfing OPCs (Figure 1F). At P9, engulfment is decreased (Figure 1G), and by P11, many microglia begin to assume a ramified morphology (Figure 1H). At P15, microglia are predominantly ramified (Figure 1I), which persists at P30 (Figure S1G), consistent with morphology found in adult brains. To assess OPC engulfment and contact by microglia, Imaris software (Bitplane) was used to analyze 3D confocal reconstructions, as described previously (Schafer et al., 2012), in three areas of the *corpus callosum* (Figure 1A). Engulfment, defined as 15% or more of NG2:Tom OPC volume internalized within microglia, peaked at P7 (Figure 1J). Contacting was defined as less than 15% of NG2:Tom OPC volume internalized within microglia (Figure S1H).

To further investigate whether microglia contained encapsulated cells consistent with data from 3D confocal imaging (Figure 1), ultrastructural assessment of the *corpus callosum* at

P7 was performed. Microglia were identified as cells with a dark, irregularly shaped nucleus (Figures 2A–2D, asterisk) and densely populated with coarse chromatin and cytoplasm (Figures 2A–2D, pseudo-colored green) with a prominent Golgi apparatus (Mori and Leblond, 1969; Sturrock, 1981; Schafer et al., 2012). Microglia were observed beginning to phagocytose a cell (Figure 2A, arrowhead). Microglia were identified with one or two fully encapsulated cells (Figures 2A–2D; arrows) consistent with confocal imaging (Figure 1). Fully engulfed cells were at varying degrees of degradation, signifying phagocytosis (Figures 2A–2D, arrows). Microglia in contact with each other (Figure 2D) were also detected, similar to confocal imaging (Figure 1F).

A marker of lysosomes specific to the myeloid lineage, CD68, was used to confirm phagocytosis (Schafer et al., 2012). Confocal 3D reconstruction shows CX3CR1:GFP microglia (Figure 2E) engulfing NG2:Tom cells (Figure 2F; merge in Figure 2G). CD68 staining (Figure 2H) shows localization of engulfed OPCs within the lysosome of microglia (Figure 2I; Video S2) and colocalization with bisbenzimide, a marker of cell nuclei (Figures 2J and 2K). The percent volume of CX3CR1:GFP microglia containing CD68+ lysosome was 56.07% ± 8.20%, and that of NG2:Tom OPCs was 29.48% ± 1.39% (Figure 2L). The percentage of engulfed NG2:Tom OPCs that colocalized with CD68 was 90.77% ± 2.32%, and the percentage of engulfed NG2:Tom OPCs that did not colocalize with CD68 was 9.23% ± 2.32% (Figure 2M). Thus, more than half the volume of ameboid microglia is occupied by the CD68+ lysosome, and more than 90% of OPCs being engulfed are inside the lysosomal compartment.

3D Confocal Reconstruction of Microglial Engulfed or Contacted OPCs Are Negative for Cell Death Markers

Apoptosis of cells or synapses signals microglial phagocytosis, regulating neural development (Sierra et al., 2010; Schafer et al., 2012). A representative confocal 3D reconstruction of CX3CR1:GFP microglia (Figure 2N) engulfing an NG2:dsRed OPC (Figure 2O; merge in Figure 2P) in the *corpus callosum* shows that the majority of OPCs are negative for caspase-3 (Figure 2Q; merge in Figure 2R), with bisbenzimide showing in blue (Figure 2S; merge in Figure 2T). The percentage of NG2:dsRed OPCs engulfed that were immunopositive for caspase-3 was 10.16% ± 2.33% (Figures 2U and S4A), whereas the percentage of NG2:dsRed OPCs engulfed that were negative for caspase-3 was 89.84% ± 2.33% (Figure 2U). Similar results were obtained for microglia contacting OPCs (Figure 2V; caspase-3-positive (+), 14.96% ± 2.99%; caspase-3-negative (−), 85.04% ± 2.99%). Therefore, the majority of OPCs engulfed or contacted by microglia were not apoptotic. NG2:dsRed-negative cells engulfed by microglia were immunopositive for caspase-3 in the cortex on P3 (Figure S4B), serving as a positive internal control because neuronal apoptosis is documented during development (Ahern et al., 2013). Additionally, caspase-3 staining was detected in the subventricular zone on P3 in a few NG2:dsRed OPCs engulfed by microglia (Figure S4C) as well as a rare NG2:dsRed OPC not in close proximity to microglia (Figure S4D). Phosphatidylserine (PS) is expressed on cells in early stages of apoptosis or cellular stress, known as an “eat me” signal in neuronal pruning (Brown and Neher, 2014). Confocal 3D reconstruction of engulfed OPCs (Figures 2W–2X; merge in Figure 2Y) shows that the majority of OPCs are negative for anti-PS (Figure 2Z; merge in

Figure 2Aa), with bisbenzimide showing in blue (Figure 2Bb; merge in Figure 2Cc). The percentage of engulfed NG2:dsRed OPCs immunopositive for anti-PS was 11.65% ± 4.77% (Figures 2Dd and S4E), whereas the percentage of NG2:dsRed OPCs engulfed that were negative for anti-PS was 88% ± 4.77% (Figure 2Dd). Similar results were obtained for microglia contacting OPCs (Figure 2Ee; anti-PS+, 15.88% ± 3.24; PS–, 84.12% ± 3.24%). In the subventricular zone at P7, a rare NG2:dsRed cell is immunopositive for anti-PS but not engulfed by microglia (Figure S4F), serving as a positive internal control. Also, a few cells negative for NG2:dsRed but positive for anti-PS were found within microglia in the subventricular zone on P7 (Figure S4G). Additionally, the cell volumes of OPCs as well as their sphericity (Figures S1I and S1J) are not different based on their interaction with microglia (engulfed or contacted) or no interactions with microglia (not contacted or engulfed). Therefore, the majority of OPCs engulfed or contacted by microglia did not appear to be undergoing cellular stress.

3D Confocal Imaging Reveals Microglia Engulfing Viable OPCs in the *Corpus Callosum* from *Ex Vivo* Brain Sections

To capture the engulfment process as well as further explore the cellular integrity of OPCs being engulfed or contacted by microglia, live 3D confocal time-lapse imaging was performed on acute *ex vivo* slices of the P7 *corpus callosum* from CX3CR1:GFP crossed with NG2:dsRed mice. Video S3 shows two different interactions of microglia with OPCs. In the first interaction, microglia contact an OPC on several occasions, but no engulfment occurs (Video S3, arrow). In the second interaction, microglia contact an OPC one or more times before engulfment (Video S3, arrowhead). 3D confocal reconstructed images from time-lapse microscopy of the *corpus callosum* in a P7 mouse brain show microglia engulfing an OPC (Figure 3A). When microglia begin to engulf an OPC, complete encapsulation occurs within 20 min (Video S4). Next, live 3D confocal time-lapse imaging of the P7 *corpus callosum* was performed in *ex vivo* slices from CX3CR1:GFP;NG2:dsRed mice in the presence of PSVue, a fluorescent dye that binds to negatively charged phospholipids such as PS, which is expressed on cells in early stages of apoptosis or cellular stress, known as an “eat me” signal in neuronal pruning (Brown and Neher, 2014). Quantification of 3D reconstructed images every 3 min over a 12-h period from four videos showed only 3 of 32 NG2:dsRed OPCs became PSVue+ before engulfment, providing evidence that the majority of OPCs were viable prior to engulfment. Only one cell became PSVue+ after engulfment; however, this happened very quickly, suggesting that it may have been in poor health prior to engulfment. The majority of cells, 28 of 32, never expressed PSVue at any point during the engulfment process. Representative 3D confocal images show that microglial engulfed OPCs (Figure 3B and 3C, arrows; merge in Figure 3D) do not express PSVue (Figure 3E; merge with dsRed only in Figure 3F; merge of all in Figure 3G; Video S5). PSVue cell debris that was not expressing dsRed was found in microglia (Figures 3B–3G, asterisks) as well as adjacent to NG2:dsRed OPCs, indicating that the dye penetrated the tissue (Video S5). To further explore the viability of OPCs during contact and engulfment by microglia, we performed 3D confocal reconstruction of *ex vivo* brain slices incubated with oxazole blue, a cell-impermeant nucleic acid stain for dead cells, and DilC1(5), a carbocyanine dye with a far-red fluorescence signal produced in the presence of mitochondrial membrane potential for viable cells. Representative 3D reconstructed images show CX3CR1:GFP

microglia engulfing NG2:dsRed OPCs (Figures 3H and 3I; merge in Figure 3J) in the P7 *corpus callosum*, which are negative for oxazole blue (Figure 3K; merge in Figure 3L). To show viable cells, DilC1(5) (Figure 3M; merge in Figure 3N), was used simultaneously, showing that engulfed OPCs are viable (Figure 3O). Arrows indicate engulfed NG2:dsRed OPCs, which are negative for oxazole blue but positive for DilC1(5). The percentage of engulfed DilC(1)5+ NG2:dsRed OPCs was 86.37% ± 4.94%, and the percentage of engulfed oxazole blue+ NG2:dsRed OPCs was 13.63% ± 4.94% (Figure 3P), providing evidence that the majority of engulfed OPCs are viable. Consistent with these data, the percentage of engulfed DilC(1)5− NG2:dsRed OPCs was 13.56% ± 4.94% (Figure 3Q), and the percentage of engulfed oxazole blue− NG2:dsRed OPCs was 85.86% ± 4.94% (Figure 3R). Likewise, the majority of contacted NG2:dsRed OPCs were DilC1(5)+ but not oxazole blue + (Figure 3S; 76.29% ± 6.75% and 23.71% ± 6.75%, respectively), supporting that engulfed and contacted OPCs by microglia are predominantly viable. Quantification of the percentage of contacted DilC1(5)− NG2:dsRed OPCs (Figure 3T; 23.71% ± 6.75%) and oxazole blue− NG2:dsRed OPCs (Figure 3U; 76.29% ± 6.75%) also corroborate that the majority of contacted OPCs are viable. Of note, no OPCs were positive for both markers, indicating specificity of the respective dyes. As a control for *ex vivo* brain sections, the percentage of engulfed OPCs quantified from 3D confocal images was compared with perfusion-fixed brain sections from CX3CR1:GFP;NG2:dsRed mice. There was no difference in engulfment from *ex vivo* brain sections compared with perfusion-fixed sections, which demonstrates that 39.18% ± 6.20% of the total NG2:dsRed OPCs are being engulfed by microglia in the *corpus callosum* (Figures S4H and S4I). Additionally, analysis of dye penetration in all OPCs and microglia is shown in Figures S4J and S4K. These data, in conjunction with live imaging data for PSVue (Figures 3B–3G) and lack of immunopositive staining for caspase-3 (Figures 2N–2V) and anti-PS (Figures 2W–2Ee) provide evidence that OPCs in the *corpus callosum* are viable before engulfment by microglia.

3D Confocal Reconstruction of the Fountain of Microglia Are Observed Engulfing OPCs before Onset of Myelination

During cerebral white matter development, OPCs are identified by expression of platelet-derived growth factor receptor alpha (PDGFRα) and chondroitin sulfate proteoglycan (NG2) (Zhu et al., 2008; Rivers et al., 2008; Dawson et al., 2003; Polito and Reynolds, 2005). OPCs differentiate into pre-myelinating oligodendrocytes, downregulate PDGFRα, but still express NG2 as well as O4 (sulfatide) and O1 (galactocerebroside) (Pfeiffer et al., 1993; Zhu et al., 2008). As pre-myelinating oligodendrocytes develop into mature oligodendrocytes, they express CC1 and myelin basic protein (MBP). The aforementioned markers were used to evaluate the maturation stage of OPCs at the time of engulfment in CX3CR1:GFP;NG2:dsRed mice. Based on live-cell imaging (Video S3) showing microglia contacting OPCs without engulfment, quantification of maturation markers in the P7 *corpus callosum* was categorized as engulfment (≥ 15% of NG2:dsRed OPC volume internalized within microglia) or contacting (<15% of NG2:dsRed OPC volume internalized within microglia). The percentage of engulfed NG2:dsRed OPCs immunopositive for NG2 was 91% when colocalized with PDGFRα (Figures 4A–4E and 4K) and 84% when colocalized with O1 (Figures 4F–4J and 4L) to yield an average of 88% (Figure 4M). Of the NG2:dsRed OPCs being engulfed, 54% were PDGFRα+/NG2+ (Figures 4K and 4M). There were no

engulfed NG2:dsRed cells that were PDGFRα+/NG2− (Figure 4K). Colocalization of NG2 with PDGFRα for NG2:dsRed OPCs contacted by microglia showed similar results (Figures S5A–S5C). Colocalization of NG2 with O1 revealed that, of the NG2:dsRed OPCs being engulfed, 55.8% were NG2+ O1+ and 8.0% were NG2− O1+ (Figure 4L). Therefore, 64% of engulfed NG2:dsRed OPCs were O1immunopositive (Figures 4L and 4M). Colocalization of NG2 with O1 for NG2:dsRed OPCs contacted by microglia showed similar results (Figures S5D–S5F). Colocalization of NG2 with CC1 demonstrated that, of the NG2:dsRed OPCs being engulfed, 18.2% were NG2+ CC1+, and 9.4% were NG2− CC1+ (Figures S5G–S5I), yielding 27% (Figure 4M). Thus, the majority of engulfed NG2:dsRed OPCs were CC1− (Figures S5G, S5H, and S6A–S6E). Colocalization of NG2 with CC1 for NG2:dsRed OPCs contacted by microglia showed similar results (Figures S5G–S5I). Additionally, there was no statistical difference between the maturation state of contacted versus engulfed NG2:dsRed OPCs (Figures S5J–S5R). Staining for MBP was found around axons that project into the cortex (Figures S6F–S6I) but sparsely found in the *corpus callosum* with no engulfment by microglia. To address the possibility of ectopic expression of genetic reporter lines as well as the multi-potency of NG2, an antibody against NG2 colocalized with multiple oligodendrocyte markers was used to confirm the oligodendrocyte lineage and expression of the reporter. Furthermore, as with most reporter lines, there is a possibility of leaky expression in other cell types. However, the majority of engulfed NG2:dsRed cells express another OPC as well as an oligodendrocyte marker. Therefore, the majority of OPCs engulfed by microglia express pre-myelinating stage markers of maturation.

3D Reconstruction of Fractalkine Receptor-Deficient Microglia Shows a Reduction in OPC Engulfment and Increased Numbers of Oligodendrocytes

The next experimental question tested whether blocking microglial phagocytosis of OPCs has a physiological effect on white matter development. The fractalkine receptor is only expressed on microglia in the CNS, and CX3CR1:GFP$^{KO/KO}$ mice are one of the most widely used tools to study modulation of synaptic engulfment during early postnatal development (Paolicelli et al., 2011; Zhan et al., 2014; Hoshiko et al., 2012). The ligand for the fractalkine receptor, CX3CL1, is expressed on developing OPCs and downregulated in mature oligodendrocytes (OLs) (Zhang et al., 2014). To determine whether fractalkine receptor deficiency in microglia alters their ability to phagocytose OPCs in the *corpus callosum* on P7, CX3CR1$^{KO/KO}$:GFP (knockout [KO]) mice were compared with CX3CR1:GFP (wild-type [WT]) mice (Figures 5A and 5B). KO mice had a statistically significant reduction in OPC engulfment (Figure 5C) but no change in contacting OPCs (Figure 5D). Furthermore, KO mice did not exhibit a change in the number or volume of microglia compared with WT mice (Figures S6J and S6K), confirming that changes in engulfment are not due to decreased numbers of microglia. To assess whether reduced microglial engulfment had a sustained effect on OL number, maturation state, or myelination, the *corpus callosum* was evaluated on P30. Cell counting revealed a statistically significant increase in the number of Olig2+ (a lineage marker; Figure 5E) and CC1+ (a mature OL marker; Figure 5F) cells in KO compared with WT mice. The corresponding representative images of Olig2 colocalized with CC1 are shown (WT: Figures 5G and 5H, merge in Figure 4I with bisbenzimide [Figure 5J] merge in Figure 5K; KO: Figures 5L and

5M, merge in Figure 5N with bisbenzimide [Figure 5O] merge in Figure 5P). Evidence that developing OPCs do not express markers of cell death or stress in fixed brains (Figures 2N–2Ee) or in *ex vivo* slices (Figures 3B–3U) in conjunction with increased number of OLs in the *corpus callosum* when microglial engulfment is blocked support that microglia engulf viable OPCs.

3D Reconstruction of Fractalkine Receptor-Deficient Microglia Shows Reduced Myelin Thickness but No Change in Axon Number

To investigate whether alterations in OL number and maturation in KO mice affect myelination, ultrastructural assessment of the P30 *corpus callosum* was performed. Representative electron microscopy (EM) images of WT *corpus callosum* show a reduction in myelin thickness in KO mice (Figures 6A and 6B; insets in Figures 6C and 6D). This was consistent with an increased g ratio (axon diameter divided by axon plus myelin diameter) in KO versus WT mice (Figure 6E). A statistically significant difference between WT and KO was observed for g ratios as a function of axon diameter (Figure 6F). A statistically significant shift in distribution toward larger g ratios (i.e., thinner myelin; Figure 6G) was observed in KO mice. Although fractalkine receptor-deficient mice exhibit an increase in extension of dopaminergic axons into the striatum during embryonic development (Squarzoni et al., 2014), we did not observe a change in axon number in the *corpus callosum* on P30 (Figure 6H). Furthermore, although there was an overall change in myelin thickness in KO mice, percentages of myelinated or unmyelinated axons were not different compared with the WT (Figures 6I and 6J). These data provide evidence that fractalkine receptor-deficient microglia reduce engulfment of, but not contact with, OPCs on P7, which increases OL number and maturation, resulting in thinner myelin compared with WT mice. These data suggest that, during development, microglia engulf OPCs at a pre-myelinating phase as a homeostatic mechanism to regulate the proper ratio of OLs per axons to promote myelination.

DISCUSSION

This study shows that the fountain of microglia phagocytoses viable OPCs in the *corpus callosum* before the onset of myelination, which may also affect cortical myelination because the *corpus callosum* is a gateway for OPC migration from the ventricular zone to the forebrain (Levison and Goldman, 1993; Kessaris et al., 2006; Crawford et al., 2016). Fractalkine receptor-deficient mice exhibit a reduction in microglial engulfment of OPCs but still contact OPCs, similar to WT mice. The inability of fractalkine receptor-deficient microglia to phagocytose OPCs results in an increase in the number of mature OLs in the *corpus callosum*, supporting the concept that OPCs are not in the process of dying before phagocytosis. Furthermore, the inability of fractalkine receptor-deficient microglia to phagocytose OPCs results in a reduction in myelin thickness in the *corpus callosum* at the ultrastructural level. These data provide evidence that microglia with an ameboid morphology in the *corpus callosum* phagocytose viable pre-myelinating OPCs in a fractalkine receptor-dependent manner as a homeostatic mechanism for proper myelin formation. Therefore, similar to microglial pruning of synapses, a proper number of OPCs, regulated by microglial pruning, is necessary for appropriate myelination.

Microglia are phagocytes of the brain that clear dead and dying cells during pathological conditions, and, more recently, they have been shown to engulf apoptotic newborn neurons during neurogenesis (Sierra et al., 2010) and caspase-3-immunopositive synapses during brain development (Schafer et al., 2012). Although it has been generally accepted that phagocytosis is preceded by cell death of the target, there is accruing evidence that microglia phagocytose viable neurons during pathological conditions (Zhao et al., 2015) as well as during development (Cunningham et al., 2013). This process, called primary phagocytosis or phagoptosis, has an important distinguishing feature in that blocking microglial engulfment prevents death of the target cell. In this regard, eliminating microglia from the fetal cerebral cortex with liposomal clodronate substantially increases the number of neuronal precursor cells in the developing cerebral cortex (Cunningham et al., 2013). Additionally, deletion of complement receptor 3-mediated microglial phagocytosis increases the number of newborn retinal ganglion cells in the embryonic mouse retina (Anderson et al., 2019). Consistent with the aforementioned studies demonstrating that blocking whole cell engulfment of live developing neurons increased their numbers, our studies show that blocking whole-cell engulfment of live OPCs increased their number in the *corpus callosum*. In our studies, the majority of OPCs engulfed by microglia in the *corpus callosum* were not immunopositive for activated caspase-3, a primary activator of apoptotic DNA fragmentation, or PS, an important “eat me” signal on cells that activates microglial phagocytosis in early stages of necrosis or apoptosis. To further explore whether OPCs that are targeted for microglial engulfment show any evidence of cell death, live confocal time-lapse imaging was performed using PSVue, a reagent containing a Zn^{2+} dipicolylamine motif that selectively binds surfaces enriched with anionic phospholipids, including PS. Our data show that the vast majority of OPCs engulfed by microglia did not express PSVue. Not only did engulfed OPCs lack expression of markers for cell death and cell stress, but the majority of them were positive for DilC1(5), a cell mitochondrial viability dye. Moreover, these *ex vivo* brain slice experiments were conducted with DilC1(5) and the cell death marker oxazole blue simultaneously, and only a small portion of engulfed or contacted OPCs were positive for oxazole blue. Evidence that OPCs do not express markers of cell death in conjunction with the increased number of OLs in the *corpus callosum* when microglial engulfment is blocked support that microglia engulf viable OPCs.

Our data show that deleting a receptor in the phagocyte system (fractalkine receptor, CX3CR1) blocks microglial engulfment of OPCs during a restricted window of development in the white matter when ameboid microglia are present (referred to as the fountain of microglia). A recent publication (Li et al., 2019) showed a proliferative region-associated subset of genes in microglia from the cerebellar white matter, consistent with the population we studied in the *corpus callosum*. However, the ability of these microglia to phagocytose was assessed with a bead assay in an *in vitro* culture system. Other studies of microglial phagocytosis of OLs have been in relationship to disease states, such as the role of CX3CR1 in microglial phagocytosis of myelin debris for proper remyelination in the cuprizone model (Lampron et al., 2015). Although blocking microglial engulfment of OPCs in fractalkine receptor-deficient mice increases the number of OLs in the *corpus callosum*, an increased number of OLs display a more mature phenotype. Another study, using pharmacological methods to render the brain devoid of microglia using intraperitoneal injection of BLZ945,

an inhibitor of colony-stimulating factor 1 receptor (Csf1r), or genetic deletion of *Csf1r*, showed a reduction in the number of mature OLs (Hagemeyer et al., 2017). We did not completely remove microglia as in the aforementioned studies but only altered the fractalkine receptor on microglia. We demonstrated that fractalkine receptor-deficient microglia exhibit a reduction in microglial engulfment of pre-myelinating OPCs but still contact OPCs, similar to WT mice. Taken together, this suggests the possibility that microglia release factors to enhance maturation of OPCs independent of their phagocytic function. One such factor may be insulin-like growth factor 1; its selective deletion from microglia impairs myelin formation in the *corpus callosum* during early postnatal development (Wlodarczyk et al., 2017).

Although our studies show that fractalkine receptor-deficient mice exhibit an increase in the number of mature OLs in the *corpus callosum*, myelin thickness is reduced at the ultrastructural level. The number of CC1+ cells in the *corpus callosum* as well as the number of Olig2+ cells were counted on P30, the same time point when EM data were analyzed. Therefore, the decrease in myelin formation cannot be due to eventual apoptosis at a later time point. This finding suggests that microglial engulfment of viable OPCs during development is important for proper myelin formation. Furthermore, on P30, the number of axons was not changed in fractalkine receptor-deficient mice compared with littermate controls. This suggests that overcrowding of OPCs, with axon numbers remaining constant, could lead to an improper balance in the ratio of OLs to the number of axons, leading to impaired myelin formation. This idea has been suggested in a zebrafish study, where reducing the number of axons resulted in a surplus of OLs (Almeida et al., 2018). Although these studies demonstrated mistargeting of myelin to neuronal cell bodies, it suggests that a proper ratio of OLs to axons is necessary for proper myelin formation. Of note, our data focus specifically on a subpopulation of ameboid microglia engulfing viable OPCs in the mouse *corpus callosum*, whose axons are distal to neuronal cell bodies in the cortex. Another study, using monocular deprivation in mice during development, observed an increase in the number of CC1+ OLs, a decrease in internode length resulting in decreased action potential conduction velocity, but no change in myelin thickness in the optic nerve and tract (Etxeberria et al., 2016). Monocular deprivation was used as a model to reduce axon function (i.e., action potential propagation) and was performed from P15–P32 in postnatal development, whereas our studies used fractalkine receptor-deficient microglia to explore the effect on engulfment of viable OPCs in the *corpus callosum* on P7, an earlier time point in development. Conditional deletion of the transcription factor EB (Class E basic helix-loop-helix protein 35) in OLs, an upstream regulator of Bax/Bak programmed cell death, results in an increase in the number of myelinated axons in the *corpus callosum* as well as in areas of the brain that are not normally myelinated, such as the molecular layer of the cerebellum (Sun et al., 2018). Our data show that blocking fractalkine-dependent engulfment of OPCs in the *corpus callosum* results in no change in the number of myelinated axons but that axons that are myelinated have thinner myelin. Although our data demonstrate that the majority of OPCs in the *corpus callosum* engulfed by microglia are viable, approximately 15% of OPCs are caspase-3-immunopositive, a marker of apoptosis, similar to published studies estimating that 20% of OPCs in the cerebral cortex degenerate by programmed cell death (Trapp et al., 1997). Although we did not observe microglia with

ameboid morphology engulfing OPCs in the cortex, which may suggest different mechanisms of OPC elimination in the *corpus callosum* compared with the cortex, our data do suggest that OPCs in the *corpus callosum* are eliminated by two different mechanisms: (1) death before microglial engulfment (apoptosis-coupled phagocytosis) and (2) alive before microglial engulfment (primary phagocytosis or phagoptosis). Although the aforementioned studies explored axon-specific or OL-specific mechanisms that regulate myelination, our data show that microglia pruning of viable OPCs also regulates myelination.

The phagocytic elimination of OPCs in this study is concurrent with a distinct population of ameboid microglia that appear in ventricular zones before term birth. This ameboid population of microglia invades the *corpus callosum* after term birth, with increasing numbers on P7 that engulf OPCs. This early postnatal time period in the rodent is consistent with the maturation stage of human perinatal white matter (Craig et al., 2003), where ameboid microglia have been described in pericallosal regions (Billiards et al., 2006; Verney et al., 2010). In preterm infants, this area of the brain, which is primarily populated with OPCs, is vulnerable to periventricular leukomalacia, predominantly characterized by diffuse reactive gliosis, loss of OLs, and relative sparing of axons, with the exception of necrotic foci (Haynes et al., 2008; Riddle et al., 2012). As shown in human post-mortem brains with periventricular leukomalacia (Billiards et al., 2008) and animal models (Segovia et al., 2008), myelination fails despite an increase in the progenitor pool. Our data presented here provide an unexplored role of pathological alterations in microglial pruning of OPCs, contributing to hypomyelination in developmental disorders.

In further support of this concept, leukodystrophies, rare genetic developmental disorders that also affect myelination, have mutations in genes important for microglial proliferation and phagocytosis. Patients with hereditary diffuse leukoencephalopathy and pigmented ortochromatic leukodystrophy have mutations in *Csf1r*, required for microglial proliferation, leading to adult-onset neurodegenerative disease (Rademakers et al., 2011; Nicholson et al., 2013; Oosterhof et al., 2019). These patients present with significant white matter atrophy, including the *corpus callosum*, and perturbed microglial morphology (Tada et al., 2016; van der Knaap and Bugiani, 2017). Similarly, Nasu-Hakola disease, a rare neurodegenerative disease characterized by early-onset dementia with sclerosing leukoencephalopathy and bone cysts, is caused by mutations of the triggering receptor expressed on myeloid cells or its adaptor protein, tyrosine kinase-binding protein (Bianchin et al., 2010), a protein complex only expressed on microglia (Jay et al., 2017). Although impaired synaptic pruning and plaque removal have been associated with altered microglial function in neurodegenerative diseases (Salter and Stevens, 2017), white matter lesions are becoming more recognized (Lee et al., 2016, 2018; Veitch et al., 2019). Clinical findings, in conjunction with data presented here, highlight the role of microglia in white matter formation, which may have long-term implications for axon integrity affecting neuronal function.

Newly generated OPCs are detected in adult demyelinating diseases, such as multiple sclerosis, but fail to form myelin. Demyelinated axons are more vulnerable to injury and lead to eventual permanent loss of neurons contributing to neurodegeneration and

progressive disability in multiple sclerosis. Therefore, remyelinating therapies are an important research focus. Studies of human post-mortem brains from individuals afflicted with multiple sclerosis show that pre-myelinating OLs are present in chronic lesions of multiple sclerosis but do not form myelin (Chang et al., 2002). Our data show that microglial pruning of OPCs is a homeostatic mechanism to regulate the number of OLs, which is critical for proper myelin sheath formation, providing a potential role of microglia as a therapeutic target for remyelinating therapies.

STAR★METHODS

Detailed methods are provided in the online version of this paper and include the following:

RESOURCE AVAILABILITY

Lead Contact—Further information and requests for resources and reagents should be directed to and will be fulfilled by the Lead Contact, Tara DeSilva (desilvt@ccf.org).

Materials Availability—This study did not generate new unique reagents

Data and Code Availability—This study did not generate/analyze datasets or codes.

EXPERIMENTAL MODEL AND SUBJECT DETAILS

Male and female mice on the C57BL/6J background were used for all experiments. The following mice were obtained from the Jackson Laboratory (Bar Harbor, ME): NG2:Tom (NG2-creER:tdTomato, Jax 008538 crossed with Jax 007914), NG2:dsRed (Jax 008241) CCR2:RFP (Jax 017586), and CX3CR1:GFP (Jax 005582). Homozygous $CX3CR1^{KO/KO}$:GFP mice are referred to as KO throughout the text, and CX3CR1:GFP mice are referred to as WT. Littermate controls were used for all experiments. Mice aged embryonic day 14 (E14), E20, postnatal day 0 (P0), P3, P4, P5, P7, P9, P11, P15 and P30 were used in this study. Animals were housed and treated in accordance with the United States National Institutes of Health guidelines for the humane treatment of animals and experiments were approved by the Institutional Animal Care and Use Committee of Cleveland Clinic.

METHOD DETAILS

Tamoxifen induction—NG2:Tom mice were injected i.p. with 10mg/mL tamoxifen (Sigma-Aldrich, St. Louis, MO; T5648) in 30μL of peanut oil at P3, with the exception of the P4 time point, which received tamoxifen at P1.

Preparation of brains for immunohistochemistry—Mice were deeply anesthetized with 5% isoflurane and transcardially perfused with phosphate buffered saline (PBS) followed by 4% paraformaldehyde (PFA). Brains were harvested and post-fixed for 24 hours in 4% PFA at 4°C, then transferred into 30% sucrose for 48 hours at 4°C. Brains were embedded in a solution of 1 part 30% sucrose in PBS and 2 parts OCT (Fisher HealthCare, Waltham, MA) and stored at −80°C. Embedded brains were sectioned into 15 μm thick coronal slices with a Leica cryostat (Leica Biosystems, Nussloch, Germany).

Immunofluorescent staining—Paraformaldehyde fixed embedded brains were sectioned and stained as recommended by antibody manufacturer. Sections were washed with PBS and blocked with 5% serum corresponding to the host of the secondary antibody with 0.3% Triton X-100 for 1 hour at room temperature. Surface antigens were stained without Triton X-100. Primary antibodies were diluted in blocking buffer and incubated overnight at 4°C. After thorough washing with PBS, sections were incubated in secondary antibodies for 1 hour at room temperature. After washing, sections were coverslipped with Fluoromount-G (Southern Biotech, Birmingham, AL; 0100–01) containing bisbenzimide (1:1000; Invitrogen, Carlsbad, CA; H3569). Primary antibodies included rabbit anti-Iba-1 (1:750; Wako, 019–19741), rabbit anti-caspase-3 (1:200; Abcam, ab32042), mouse anti-phosphatidylserine (1:200 without triton; Millipore, 05–719), mouse anti-CD68 (1:200; Biorad, mca1957 ga), rat anti-PDGFRα (1:400; BD Biosciences, 558774), rabbit anti-NG2 (1:200 free-floating; Millipore, ab5320), mouse anti-O1 (1:100 free-floating without triton; Millipore, mab344), mouse anti-CC1 (1:100; Millipore, OP80), rat anti-MBP (1:400; Abcam, ab7349) and rabbit anti-Olig2 (1:200; Millipore, ab9610). Secondary antibodies included Alexa Fluor 488 goat anti-rabbit IgG (1:1000; Invitrogen, A11034), Alexa Fluor 647 goat anti-rabbit IgG (1:1000; Invitrogen, A21245), Alexa Fluor 647 goat anti-mouse IgG (1:1000; Invitrogen, A21235), Alexa Flour 647 goat anti-rat (1:1000; Invitrogen, A21247), Biotinylated goat anti-rabbit IgG (1:200; Vector Labs, BA-1000 used with 405 conjugated streptavidin DyLight 1:1000; Thermo Scientific, 21831), and Alexa Fluor 647 goat anti-mouse IgM (1:500; Abcam, ab150123).

Confocal 3D time-lapse microscopy in ex-vivo slices—Transgenic mice with CX3CR1:GFP and NG2:dsRed reporters were sacrificed at P7 for live imaging experiments. Brains were rapidly harvested and placed in artificial CSF solution (aCSF containing NaCl 126 mM, $NaHCO_3$ 26 mM, KCl 3.0 mM, NaH_2PO_4 1.25 mM, Mg_2SO_4 2.0 mM, $CaCl_2$ 2.0 mM, 10mM dextrose, pH 7.4) and sectioned coronally on ice into 300μm-thick sections with a vibrating microtome (Leica, Heidelberg, Germany). Brain slices were bubbled in aCSF with carbogen (95%O_2, 5%CO_2) for 60 minutes at room temperature before being transferred into a heat and CO_2 incubated live-cell imaging chamber containing aCSF on an inverted Leica confocal microscope for long-term imaging. Image stacks were taken at 40× magnification in 2 fields of view per slice, every 4 minutes for a duration of 12 hours for live imaging observation. Image stacks were 3D reconstructed in Imaris software (Bitplane, Zurich, Switzerland). *Ex-vivo* brain slices used in live imaging experiments from P7 transgenic mice with CX3CR1:GFP and NG2:dsRed reporters were incubated in PSVue dye (PSVue-643, Molecular Targeting Technologies Inc., West Chester, PA) to determine if OPCs were stressed or dying prior to engulfment. PSVue is a fluorescent dye that binds to negatively charged phospholipids such as phosphatidylserine, which are exposed to the outer leaflet of the cell membrane in early stages of apoptosis or cellular stress, and is an “eat-me” signal in neuronal pruning. Slices were prepared as described above. PSVue-643 was diluted in aCSF at 5μM and *ex-vivo* slices were incubated for 20 minutes prior to live imaging acquisition. Image stacks were taken at 40× magnification in 2 fields of view per slice, every 3 minutes for a duration of 12 hours. Image stacks were 3D reconstructed in Imaris software (Bitplane, Zurich, Switzerland) and compressed to tiff stacks of the time series to be annotated in ImageJ software. Cells were considered engulfed when 100% of their cell body

was inside of a microglial cell, which was confirmed in Imaris 3D reconstructed videos. Engulfed cells were characterized by PSVue positivity before or after engulfment.

Imaging—Images were acquired using a Nikon C2 confocal microscope with NIS-Elements software (Nikon, Melville, NY). Image stacks for 3D reconstruction were captured at 15 μm thickness using 0.3 μm step size with a Plan Fluor 40X/1.30 NA (oil immersion) objective from three areas of the corpus callosum (Figure 1 A, boxes). Live imaging studies were conducted using a Leica TCS-SP8-AOBS inverted confocal microscope (Leica Microsystems, GmbH, Wetzlar, Germany) with a Plan Apo 40×/1.25 NA objective (Leica Microsystems, Wetzlar, Germany). Electron microscopy studies were evaluated on a Tecnai G2 SpiritBT transmission electron microscope (FEI Company, Hillsboro, OR) operated at 60 kV.FEI Tecnai Spirit (T12) with a Gatan US4000 4kx4k CCD.

Electron microscopy—Mice were deeply anesthetized and 100 μL of 1% lidocaine was injected into the left lateral ventricle prior to transcardial perfusion with 20mL of 37°C quarter-strength Karnovsky's fixative solution at a flow rate of 10 mL/min for 10 minutes. Brains were harvested and sectioned 500 μm-thick (coronally at P7, sagittally at P30) with a vibrating microtome (Leica, Heidelberg, Germany). A 500 μm x 500 μm cube was cut from the corpus callosum above the lateral ventricle where all confocal images were collected and fixed by immersion in triple-aldehyde DMSO (Fujioka et al., 2014a, 2014b). Specimen were thoroughly rinsed in 0.1 M phosphate buffer, pH 7.4, then post-fixed for 2 hours in an unbuffered 1:1 mixture of 2% osmium tetroxide and 3% potassium ferricyanide. After rinsing with distilled water, the specimen were soaked overnight in an acidified solution of 0.25% uranyl acetate. After another rinse in distilled water, they were dehydrated in ascending concentrations of ethanol, passed through propylene oxide, and embedded in Embed-812 resin mixture (Electron Microscopy Sciences, Hatfield, PA). Thin sections were sequentially stained with acidified uranyl acetate followed by a modification of Sato's triple lead stain and examined in a FEI Tecnai Spirit (T12) with a Gatan US4000 4kx4k CCD.

QUANTIFICATION AND STATISTICAL ANALYSIS

Quantification of CD68 colocalization—Coronal sections from P7 CX3CR1:GFP;NG2:Tom mice were stained for CD68 and analyzed beginning at the level of the lateral ventricles with 9 z stacks per animal from 3 serial sections including every 10^{th} serial 15 μm section. Confocal z stacks were taken at 40X magnification with 200 μm x 200 μm x 15 μm fields. Manual thresholding was used to create surface renders of each channel with NIS-Elements software (Nikon, Melville, NY) in a blinded manner. The percentage of microglial volume that was filled with CD68+ lysosome staining and NG2:Tom+ cell volume was quantified as previously described in studies on synapse engulfment (Schafer et al., 2012). Additionally, the NG2:Tom+ cells engulfed by microglia were categorized as being positive or negative for CD68 staining.

Engulfment analysis—Microglial engulfment of OPCs was assessed using methods adapted from previous work studying synaptic pruning (Schafer et al., 2012). Confocal z stacks of paraformaldehyde fixed brains and *ex-vivo* brain slices were imported into Imaris software (Bitplane, Zurich, Switzerland) as 3D reconstructions. Surface rendering was

conducted on microglia and OPCs using 0.1 μm and 0.4 μm smoothing, respectively, and absolute thresholding was utilized in a blinded manner. Surfaces smaller than 10 μm^3 were filtered out. Surface renders were manually separated or unified as necessary using bisbenzimide as a marker of the cell nucleus. This effectively eliminated microglial processes in other planes from the analysis. OPC surface rendering also filtered out any surfaces with a volume less than 10 μm^3 and sphericity value lower than 0.49 to exclude pericytes on blood vessels that express the NG2 marker. These criteria were determined based on the size of pericytes on blood vessels as reported (Peppiatt et al., 2006). Once surface renders were complete, the surface-surface coloc XTension software available through Imaris was used to create a new surface channel which identifies overlapping voxels between microglia and OPC surfaces. The microglia to OPC surface volumes were divided by their corresponding OPC volumes to determine the percentage of OPC internalized within microglia. Based on live cell imaging (Video S3) showing microglia contacting OPCs without engulfment, quantification was categorized as engulfment (≥ 15% of NG2:dsRed OPC volume internalized by microglia) or contacting (< 15% of NG2:dsRed OPC volume internalized by microglia).

Quantification of cell death markers in fixed tissue—Coronal brain sections from P7 paraformaldehyde-fixed CX3CR1:GFP;NG2:dsRed mice were stained with antibodies generated against caspase-3 and phosphatidylserine and analyzed beginning at the level of the lateral ventricles with 4 z stacks per animal from 3 serial sections including every 10^{th} serial 15 μm section. 3D Confocal z stacks were taken at 40X magnification with 200 μm × 200 μm × 15 μm fields. Using Imaris software (Bitplane, Zurich, Switzerland), images were analyzed for OPC engulfment or contact by microglia as specified in the “Engulfment analysis” method above. Engulfed or contacted OPCs were classified as being immunopositive or negative for caspase-3 or phosphatidylserine staining.

Quantification of oligodendrocyte maturation—Coronal brain sections from P7 paraformaldehyde-fixed CX3CR1:GFP;NG2:dsRed mice were double-stained for maturation markers. Sections were analyzed beginning at the level of the lateral ventricles with 3 z stacks per animal from 3 serial sections including every 10^{th} serial 15 μm section for quantification. 3D Confocal z stacks were taken at 40X magnification with 0.3 μm step and 204 μm x 204 μm x 15 μm fields. Using Imaris software (Bitplane, Zurich, Switzerland), images were analyzed for OPC engulfment or contact by microglia as specified in the “Engulfment analysis” method above. Engulfed and contacted OLs were classified by immunopositive staining for PDGFRα+/NG2-; PDGFRα+/NG2+; PDGFRα-/NG2+; or NG2+/O1-; NG2+/O1+; NG2-/O1+; or NG2+/CC1-; NG2+/CC1+; NG2-/CC1+.

Quantification of engulfment in CX3CR1 KO mice—Coronal brain sections 15 μm-thick from P7 paraformaldehyde-fixed $CX3CR1^{KO/KO}$:GFP;NG2:Tom (KO) and CX3CR1:GFP;NG2:Tom (WT) mice were collected beginning at the level of the lateral ventricles with 9 z stacks per animal from 3 serial sections including every 10^{th} serial section for quantification. 3D Confocal z stacks were taken at 40X magnification with 0.3 μm step and 204 μm x 204 μm x 15 μm fields. Using Imaris software (Bitplane, Zurich,

Switzerland), images were analyzed for OPC engulfment or contact by microglia as specified in the “Engulfment analysis” method above.

Quantification of oligodendrocyte number at P30—Cell counts were conducted on coronal brain sections from the corpus callosum of paraformaldehyde-fixed P30 CX3CR1$^{KO/KO}$:GFP (KO) and P30 CX3CR1:GFP (WT) mice stained for CC1, a marker of mature OLs, and Olig2, a marker of all OLs. Coronal sections 15 μm-thick were analyzed beginning at the level of the lateral ventricles with 6 images per animal from 3 serial sections including every 10th serial section for quantification. Images were taken at 20X magnification with 204 μm x 204 μm fields. Cells were counted as positive for Olig2 or CC1 using the cell counter plugin with free NIH software (ImageJ). All cells counted were confirmed to have a bisbenzimide-positive nucleus.

Quantification of cell viability in ex-vivo slices—Oxazole blue/DilC1(5) dyes (oxazole blue 455, DilC1(5) 658, Biotium Inc., Fremont, CA) were used in acute experiments with *ex-vivo* brain slices to confirm cell viability of engulfed and contacted cells. Oxazole blue, also known as PO-PRO-1 is a cell-impermeant nucleic acid stain for dead cells fluorescing in blue. DilC1(5) is a carbocyanine dye with far-red fluorescence signal produced in the presence of mitochondrial membrane potential, such that decreased fluorescence signal is observed in apoptotic cells. Oxazole blue was diluted to 1μM and DilC1(5) was diluted to 100nM in aCSF and *ex-vivo* slices were incubated for 20 minutes prior to 3D confocal microscopy acquisition. Dyes were used simultaneously to observe cell viability versus death in engulfed OPCs. Image stacks were taken at 40× magnification in 2 fields of view per slice. Image stacks were 3D reconstructed in Imaris software (Bitplane, Zurich, Switzerland) and analyzed for OPC engulfment or contact by microglia as specified in the “Engulfment analysis” method above. Engulfed and contacted OPCs were characterized by their positivity for NG2:dsRed and immunopositive staining for DilC1(5), and/or oxazole blue.

Analysis of electron microscopy—To observe engulfment at the ultrastructural level, brain sections from the corpus callosum of CX3CR1:GFP;NG2:Tom (WT) mice was examined with electron microscopy at P7. To evaluate myelination changes in fractalkine receptor-deficient mice, brain tissue from the corpus callosum of P30 CX3CR1$^{KO/KO}$:GFP (KO) and CX3CR1:GFP (WT) mice was imaged using electron microscopy and g ratios and axon numbers were analyzed. Ten images per mouse taken at 6800X magnification (20.75 μm x 13.68 μm) were used to measure g-ratios and count axons. All data was analyzed blinded. Axons were counted using the cell counter plugin with Fiji software (ImageJ) and characterized as unmyelinated or myelinated based on the presence of dark bands surrounding microtubule-containing axons. Myelinated axons in each image were traced using the tracing tool to create ROIs in Fiji and determine the diameter of the axon and the myelin with the axon inside of it. The g-ratios were calculated as axon diameter divided by axon plus myelin diameter. All axons in each image were counted and calculated as number of axons per mm^2.

Statistical analyses—All statistical analyses were performed with GraphPad Prism software version 5.03 (GraphPad Software, La Jolla, CA) or IBM SPSS version 25 (IBM Corp., Armonk, NY). Specific analyses performed including *p* values are reported where indicated in the figure legends and results.

Supplementary Material

Refer to Web version on PubMed Central for supplementary material.

ACKNOWLEDGMENTS

We would like to thank Judith Drazba, Director of the Cleveland Clinic Imaging core, for assistance with live imaging and electron microscopy and Hisashi Fujioka, Director of the Case Western Reserve University Cryo-Electron Microscopy core for assistance with electron microscopy. We also thank Terri O'Brian, Mary Reagan, and Dave Schumick from the Cleveland Clinic Center for Medical Art & Photography for assistance with figure illustrations. This study was supported by National Multiple Sclerosis Society RG 4587-A-1, National Science Foundation 1648822, National Eye Institute RO1EY025687, and the Mike L. Jezdimir Transverse Myelitis Foundation. This work utilized the Leica SP8 confocal microscope that was purchased with funding from National Institutes of Health SIG grant 1S10OD019972–01.

REFERENCES

Adlaf EW, Vaden RJ, Niver AJ, Manuel AF, Onyilo VC, Araujo MT, Dieni CV, Vo HT, King GD, Wadiche JI, and Overstreet-Wadiche L (2017). Adult-born neurons modify excitatory synaptic transmission to existing neurons. eLife 6, e19886. [PubMed: 28135190]

Ahern TH, Krug S, Carr AV, Murray EK, Fitzpatrick E, Bengston L, McCutcheon J, De Vries GJ, and Forger NG (2013). Cell death atlas of the postnatal mouse ventral forebrain and hypothalamus: effects of age and sex. J. Comp. Neurol 521, 2551–2569. [PubMed: 23296992]

Almeida RG, Pan S, Cole KLH, Williamson JM, Early JJ, Czopka T, Klingseisen A, Chan JR, and Lyons DA (2018). Myelination of Neuronal Cell Bodies when Myelin Supply Exceeds Axonal Demand. Curr. Biol 28, 1296–1305.e5. [PubMed: 29628374]

Anderson SR, Zhang J, Steele MR, Romero CO, Kautzman AG, Schafer DP, and Vetter ML (2019). Complement Targets Newborn Retinal Ganglion Cells for Phagocytic Elimination by Microglia. J. Neurosci 39, 2025–2040. [PubMed: 30647151]

Bianchin MM, Martin KC, De Souza AC, De Oliveira MA, and Rieder CR (2010). Nasu-Hakola disease and primary microglial dysfunction. Nat. Rev. Neurol 6, 2 p following 523. [PubMed: 20836191]

Billiards SS, Haynes RL, Folkerth RD, Trachtenberg FL, Liu LG, Volpe JJ, and Kinney HC (2006). Development of microglia in the cerebral white matter of the human fetus and infant. J. Comp. Neurol 497, 199–208. [PubMed: 16705680]

Billiards SS, Haynes RL, Folkerth RD, Borenstein NS, Trachtenberg FL, Rowitch DH, Ligon KL, Volpe JJ, and Kinney HC (2008). Myelin abnormalities without oligodendrocyte loss in periventricular leukomalacia. Brain Pathol. 18, 153–163. [PubMed: 18177464]

Brown GC, and Neher JJ (2014). Microglial phagocytosis of live neurons. Nat. Rev. Neurosci 15, 209–216. [PubMed: 24646669]

Chang A, Tourtellotte WW, Rudick R, and Trapp BD (2002). Premyelinating oligodendrocytes in chronic lesions of multiple sclerosis. N. Engl. J. Med 346, 165–173. [PubMed: 11796850]

Craig A, Ling Luo N, Beardsley DJ, Wingate-Pearse N, Walker DW, Hohimer AR, and Back SA (2003). Quantitative analysis of perinatal rodent oligodendrocyte lineage progression and its correlation with human. Exp. Neurol 181, 231–240. [PubMed: 12781996]

Crawford AH, Tripathi RB, Richardson WD, and Franklin RJM (2016). Developmental Origin of Oligodendrocyte Lineage Cells Determines Response to Demyelination and Susceptibility to Age-Associated Functional Decline. Cell Rep. 15, 761–773. [PubMed: 27149850]

Cunningham CL, Martínez-Cerdeño V, and Noctor SC (2013). Microglia regulate the number of neural precursor cells in the developing cerebral cortex. J. Neurosci 33, 4216–4233. [PubMed: 23467340]

Davalos D, Grutzendler J, Yang G, Kim JV, Zuo Y, Jung S, Littman DR, Dustin ML, and Gan WB (2005). ATP mediates rapid microglial response to local brain injury in vivo. Nat. Neurosci 8, 752–758. [PubMed: 15895084]

Dawson MR, Polito A, Levine JM, and Reynolds R (2003). NG2-expressing glial progenitor cells: an abundant and widespread population of cycling cells in the adult rat CNS. Mol. Cell. Neurosci 24, 476–488. [PubMed: 14572468]

Etxeberria A, Hokanson KC, Dao DQ, Mayoral SR, Mei F, Redmond SA, Ullian EM, and Chan JR (2016). Dynamic Modulation of Myelination in Response to Visual Stimuli Alters Optic Nerve Conduction Velocity. J. Neurosci 36, 6937–6948. [PubMed: 27358452]

Filipello F, Morini R, Corradini I, Zerbi V, Canzi A, Michalski B, Erreni M, Markicevic M, Starvaggi-Cucuzza C, Otero K, et al. (2018). The Microglial Innate Immune Receptor TREM2 Is Required for Synapse Elimination and Normal Brain Connectivity. Immunity 48, 979–991.e8. [PubMed: 29752066]

Fujioka H, Tandler B, Cohen M, Koontz D, and Hoppel CL (2014a). Multiple mitochondrial alterations in a case of myopathy. Ultrastruct. Pathol 38, 204–210. [PubMed: 24579828]

Fujioka H, Tandler B, Rosca M, McCandless SE, Katirji B, Cohen ML, Rapisuwon S, and Hoppel CL (2014b). Multiple muscle cell alterations in a case of encephalomyopathy. Ultrastruct. Pathol 38, 13–25. [PubMed: 24134831]

Fünfschilling U, Supplie LM, Mahad D, Boretius S, Saab AS, Edgar J, Brinkmann BG, Kassmann CM, Tzvetanova ID, Möbius W, et al. (2012). Glycolytic oligodendrocytes maintain myelin and long-term axonal integrity. Nature 485, 517–521. [PubMed: 22622581]

Ginhoux F, Greter M, Leboeuf M, Nandi S, See P, Gokhan S, Mehler MF, Conway SJ, Ng LG, Stanley ER, et al. (2010). Fate mapping analysis reveals that adult microglia derive from primitive macrophages. Science 330, 841–845. [PubMed: 20966214]

Gomez Perdiguero E, Klapproth K, Schulz C, Busch K, Azzoni E, Crozet L, Garner H, Trouillet C, de Bruijn MF, Geissmann F, and Rodewald HR (2015). Tissue-resident macrophages originate from yolk-sac-derived erythromyeloid progenitors. Nature 518, 547–551. [PubMed: 25470051]

Hagemeyer N, Hanft KM, Akriditou MA, Unger N, Park ES, Stanley ER, Staszewski O, Dimou L, and Prinz M (2017). Microglia contribute to normal myelinogenesis and to oligodendrocyte progenitor maintenance during adulthood. Acta Neuropathol. 134, 441–458. [PubMed: 28685323]

Haynes RL, Billiards SS, Borenstein NS, Volpe JJ, and Kinney HC (2008). Diffuse axonal injury in periventricular leukomalacia as determined by apoptotic marker fractin. Pediatr. Res 63, 656–661. [PubMed: 18520330]

Hoshiko M, Arnoux I, Avignone E, Yamamoto N, and Audinat E (2012). Deficiency of the microglial receptor CX3CR1 impairs postnatal functional development of thalamocortical synapses in the barrel cortex. J. Neurosci 32, 15106–15111. [PubMed: 23100431]

Imamoto K, and Leblond CP (1978). Radioautographic investigation of gliogenesis in the corpus callosum of young rats. II. Origin of microglial cells. J. Comp. Neurol 180, 139–163. [PubMed: 649786]

Jay TR, von Saucken VE, and Landreth GE (2017). TREM2 in Neurodegenerative Diseases. Mol. Neurodegener 12, 56. [PubMed: 28768545]

Kessaris N, Fogarty M, Iannarelli P, Grist M, Wegner M, and Richardson WD (2006). Competing waves of oligodendrocytes in the forebrain and postnatal elimination of an embryonic lineage. Nat. Neurosci 9, 173–179. [PubMed: 16388308]

Lampron A, Larochelle A, Laflamme N, Préfontaine P, Plante MM, Sánchez MG, Yong VW, Stys PK, Tremblay ME, and Rivest S (2015). Inefficient clearance of myelin debris by microglia impairs remyelinating processes. J. Exp. Med 212, 481–495. [PubMed: 25779633]

Lee Y, Morrison BM, Li Y, Lengacher S, Farah MH, Hoffman PN, Liu Y, Tsingalia A, Jin L, Zhang PW, et al. (2012). Oligodendroglia metabolically support axons and contribute to neurodegeneration. Nature 487, 443–448. [PubMed: 22801498]

Lee S, Viqar F, Zimmerman ME, Narkhede A, Tosto G, Benzinger TL, Marcus DS, Fagan AM, Goate A, Fox NC, et al.; Dominantly Inherited Alzheimer Network (2016). White matter hyperintensities

are a core feature of Alzheimer's disease: Evidence from the dominantly inherited Alzheimer network. Ann. Neurol 79, 929–939. [PubMed: 27016429]

Lee S, Zimmerman ME, Narkhede A, Nasrabady SE, Tosto G, Meier IB, Benzinger TLS, Marcus DS, Fagan AM, Fox NC, et al.; Dominantly Inherited Alzheimer Network (2018). White matter hyperintensities and the mediating role of cerebral amyloid angiopathy in dominantly-inherited Alzheimer's disease. PLoS ONE 13, e0195838. [PubMed: 29742105]

Levison SW, and Goldman JE (1993). Both oligodendrocytes and astrocytes develop from progenitors in the subventricular zone of postnatal rat forebrain. Neuron 10, 201–212. [PubMed: 8439409]

Li Q, Cheng Z, Zhou L, Darmanis S, Neff NF, Okamoto J, Gulati G, Bennett ML, Sun LO, Clarke LE, et al. (2019). Developmental Heterogeneity of Microglia and Brain Myeloid Cells Revealed by Deep Single-Cell RNA Sequencing. Neuron 101, 207–223.e10. [PubMed: 30606613]

Ling EA (1979). Transformation of monocytes into amoeboid microglia in the corpus callosum of postnatal rats, as shown by labelling monocytes by carbon particles. J. Anat 128, 847–858. [PubMed: 489472]

Mizutani M, Pino PA, Saederup N, Charo IF, Ransohoff RM, and Cardona AE (2012). The fractalkine receptor but not CCR2 is present on microglia from embryonic development throughout adulthood. J. Immunol 188, 29–36. [PubMed: 22079990]

Mori S, and Leblond CP (1969). Identification of microglia in light and electron microscopy. J. Comp. Neurol 135, 57–80. [PubMed: 4181000]

Nicholson AM, Baker MC, Finch NA, Rutherford NJ, Wider C, Graff-Radford NR, Nelson PT, Clark HB, Wszolek ZK, Dickson DW, et al. (2013). CSF1R mutations link POLD and HDLS as a single disease entity. Neurology 80, 1033–1040. [PubMed: 23408870]

Nimmerjahn A, Kirchhoff F, and Helmchen F (2005). Resting microglial cells are highly dynamic surveillants of brain parenchyma in vivo. Science 308, 1314–1318. [PubMed: 15831717]

Oosterhof N, Chang IJ, Karimiani EG, Kuil LE, Jensen DM, Daza R, Young E, Astle L, van der Linde HC, Shivaram GM, et al. (2019). Homozygous Mutations in CSF1R Cause a Pediatric-Onset Leukoencephalopathy and Can Result in Congenital Absence of Microglia. Am. J. Hum. Genet 104, 936–947. [PubMed: 30982608]

Paolicelli RC, Bolasco G, Pagani F, Maggi L, Scianni M, Panzanelli P, Giustetto M, Ferreira TA, Guiducci E, Dumas L, et al. (2011). Synaptic pruning by microglia is necessary for normal brain development. Science 333, 1456–1458. [PubMed: 21778362]

Peppiatt CM, Howarth C, Mobbs P, and Attwell D (2006). Bidirectional control of CNS capillary diameter by pericytes. Nature 443, 700–704. [PubMed: 17036005]

Pfeiffer SE, Warrington AE, and Bansal R (1993). The oligodendrocyte and its many cellular processes. Trends Cell Biol. 3, 191–197. [PubMed: 14731493]

Polito A, and Reynolds R (2005). NG2-expressing cells as oligodendrocyte progenitors in the normal and demyelinated adult central nervous system. J. Anat 207, 707–716. [PubMed: 16367798]

Rademakers R, Baker M, Nicholson AM, Rutherford NJ, Finch N, Soto-Ortolaza A, Lash J, Wider C, Wojtas A, DeJesus-Hernandez M, et al. (2011). Mutations in the colony stimulating factor 1 receptor (CSF1R) gene cause hereditary diffuse leukoencephalopathy with spheroids. Nat. Genet 44, 200–205. [PubMed: 22197934]

Riddle A, Maire J, Gong X, Chen KX, Kroenke CD, Hohimer AR, and Back SA (2012). Differential susceptibility to axonopathy in necrotic and nonnecrotic perinatal white matter injury. Stroke 43, 178–184. [PubMed: 22076007]

Rivers LE, Young KM, Rizzi M, Jamen F, Psachoulia K, Wade A, Kessaris N, and Richardson WD (2008). PDGFRA/NG2 glia generate myelinating oligodendrocytes and piriform projection neurons in adult mice. Nat. Neurosci 11, 1392–1401. [PubMed: 18849983]

Saederup N, Cardona AE, Croft K, Mizutani M, Cotleur AC, Tsou CL, Ransohoff RM, and Charo IF (2010). Selective chemokine receptor usage by central nervous system myeloid cells in CCR2-red fluorescent protein knock-in mice. PLoS ONE 5, e13693. [PubMed: 21060874]

Salter MW, and Stevens B (2017). Microglia emerge as central players in brain disease. Nat. Med 23, 1018–1027. [PubMed: 28886007]

Schafer DP, Lehrman EK, Kautzman AG, Koyama R, Mardinly AR, Yamasaki R, Ransohoff RM, Greenberg ME, Barres BA, and Stevens B (2012). Microglia sculpt postnatal neural circuits in an activity and complement-dependent manner. Neuron 74, 691–705. [PubMed: 22632727]

Segovia KN, McClure M, Moravec M, Luo NL, Wan Y, Gong X, Riddle A, Craig A, Struve J, Sherman LS, and Back SA (2008). Arrested oligodendrocyte lineage maturation in chronic perinatal white matter injury. Ann. Neurol 63, 520–530. [PubMed: 18393269]

Sierra A, Encinas JM, Deudero JJ, Chancey JH, Enikolopov G, Overstreet-Wadiche LS, Tsirka SE, and Maletic-Savatic M (2010). Microglia shape adult hippocampal neurogenesis through apoptosis-coupled phagocytosis. Cell Stem Cell 7, 483–495. [PubMed: 20887954]

Smith RS, and Koles ZJ (1970). Myelinated nerve fibers: computed effect of myelin thickness on conduction velocity. Am. J. Physiol 219, 1256–1258. [PubMed: 5473105]

Squarzoni P, Oller G, Hoeffel G, Pont-Lezica L, Rostaing P, Low D, Bessis A, Ginhoux F, and Garel S (2014). Microglia modulate wiring of the embryonic forebrain. Cell Rep. 8, 1271–1279. [PubMed: 25159150]

Sturrock RR (1981). Microglia in the prenatal mouse neostriatum and spinal cord. J. Anat 133, 499–512. [PubMed: 7333957]

Sun LO, Mulinyawe SB, Collins HY, Ibrahim A, Li Q, Simon DJ, Tessier-Lavigne M, and Barres BA (2018). Spatiotemporal Control of CNS Myelination by Oligodendrocyte Programmed Cell Death through the TFEBPUMA Axis. Cell 175, 1811–1826.e21. [PubMed: 30503207]

Tada M, Konno T, Tada M, Tezuka T, Miura T, Mezaki N, Okazaki K, Arakawa M, Itoh K, Yamamoto T, et al. (2016). Characteristic microglial features in patients with hereditary diffuse leukoencephalopathy with spheroids. Ann. Neurol 80, 554–565. [PubMed: 27490250]

Trapp BD, Nishiyama A, Cheng D, and Macklin W (1997). Differentiation and death of premyelinating oligodendrocytes in developing rodent brain. J. Cell Biol 137, 459–468. [PubMed: 9128255]

Ueno M, Fujita Y, Tanaka T, Nakamura Y, Kikuta J, Ishii M, and Yamashita T (2013). Layer V cortical neurons require microglial support for survival during postnatal development. Nat. Neurosci 16, 543–551. [PubMed: 23525041]

van der Knaap MS, and Bugiani M (2017). Leukodystrophies: a proposed classification system based on pathological changes and pathogenetic mechanisms. Acta Neuropathol. 134, 351–382. [PubMed: 28638987]

Veitch DP, Weiner MW, Aisen PS, Beckett LA, Cairns NJ, Green RC, Harvey D, Jack CR Jr., Jagust W, Morris JC, et al.; Alzheimer's Disease Neuroimaging Initiative (2019). Understanding disease progression and improving Alzheimer's disease clinical trials: Recent highlights from the Alzheimer's Disease Neuroimaging Initiative. Alzheimers Dement. 15, 106–152. [PubMed: 30321505]

Verney C, Monier A, Fallet-Bianco C, and Gressens P (2010). Early microglial colonization of the human forebrain and possible involvement in periventricular white-matter injury of preterm infants. J. Anat 217, 436–448. [PubMed: 20557401]

Vinet J, Weering HR, Heinrich A, Kälin RE, Wegner A, Brouwer N, Heppner FL, Rooijen N.v., Boddeke HW, and Biber K (2012). Neuroprotective function for ramified microglia in hippocampal excitotoxicity. J. Neuroinflammation 9, 27. [PubMed: 22293457]

Wlodarczyk A, Holtman IR, Krueger M, Yogev N, Bruttger J, Khorooshi R, Benmamar-Badel A, de Boer-Bergsma JJ, Martin NA, Karram K, et al. (2017). A novel microglial subset plays a key role in myelinogenesis in developing brain. EMBO J. 36, 3292–3308. [PubMed: 28963396]

Zhan Y, Paolicelli RC, Sforazzini F, Weinhard L, Bolasco G, Pagani F, Vyssotski AL, Bifone A, Gozzi A, Ragozzino D, and Gross CT (2014). Deficient neuron-microglia signaling results in impaired functional brain connectivity and social behavior. Nat. Neurosci 17, 400–406. [PubMed: 24487234]

Zhang Y, Chen K, Sloan SA, Bennett ML, Scholze AR, O'Keeffe S, Phatnani HP, Guarnieri P, Caneda C, Ruderisch N, et al. (2014). An RNA-sequencing transcriptome and splicing database of glia, neurons, and vascular cells of the cerebral cortex. J. Neurosci 34, 11929–11947. [PubMed: 25186741]

Zhao L, Zabel MK, Wang X, Ma W, Shah P, Fariss RN, Qian H, Parkhurst CN, Gan WB, and Wong WT (2015). Microglial phagocytosis of living photoreceptors contributes to inherited retinal degeneration. EMBO Mol. Med 7, 1179–1197. [PubMed: 26139610]

Zhu X, Bergles DE, and Nishiyama A (2008). NG2 cells generate both oligodendrocytes and gray matter astrocytes. Development 135, 145–157. [PubMed: 18045844]

Highlights

- Ameboid microglia invade the *corpus callosum* and engulf OPCs during development
- Majority of OPCs engulfed by ameboid microglia in the *corpus callosum* are viable
- Fractalkine receptor-deficient microglia exhibit a reduction in engulfment of OPCs
- Fractalkine receptor-deficient mice have reduced myelin thickness in adulthood

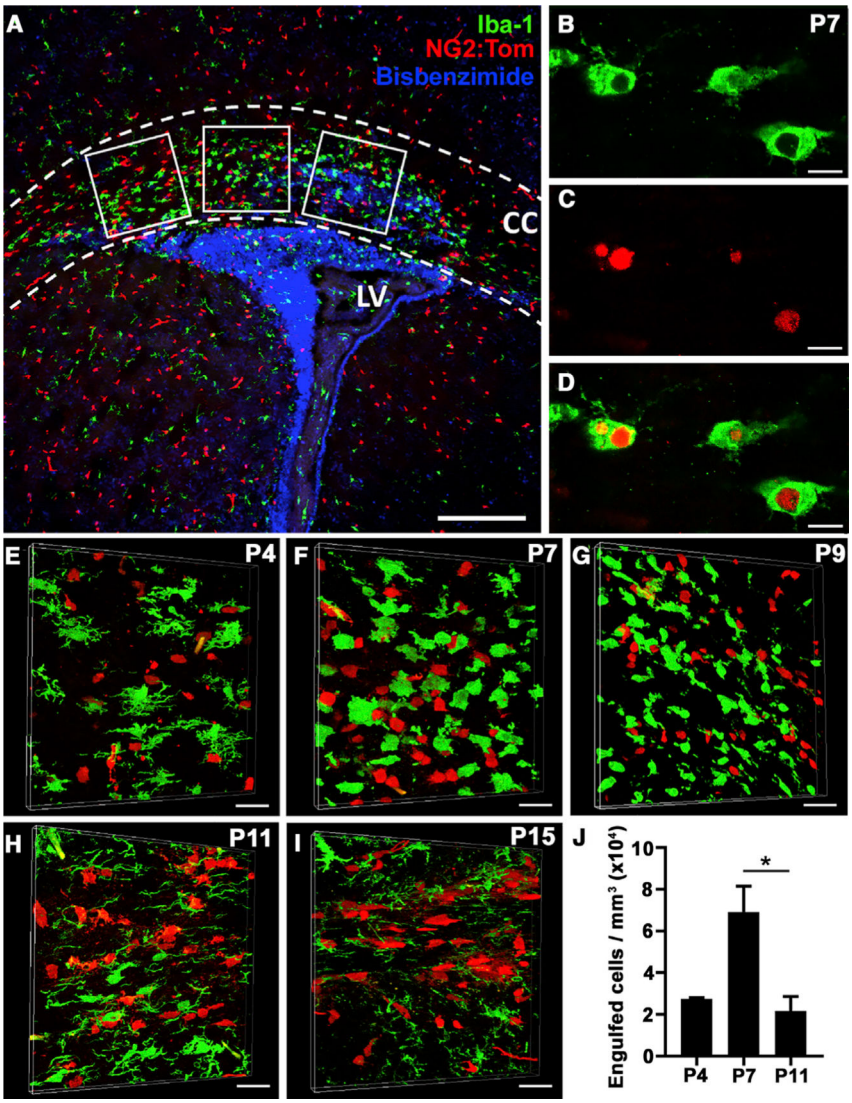

Figure 1. Ameboid Microglia in the Corpus Callosum Engulf OL Progenitor Cells (OPCs) on Post-natal Day 7 (P7)

(A) Representative image of a P7 mouse *corpus callosum* (CC), outlined by a dotted line above the lateral ventricle (LV), from a NG2:Tom mouse (OPCs, red) co-localized with the myeloid lineage marker Iba-1 (microglia, green) and bisbenzimide (blue) to identify nuclei. White boxes depict areas analyzed by 3D reconstruction. Scale bar, 200 μm.

(B–D) A 0.3-μm plane from a 3D confocal z stack showing ameboid microglia (B) engulfing NG2:Tom OPCs (C) in a merged image with red OPCs inside of green microglia (D). Scale bars, 10 μm.

(E–I) Microglia display distinct morphological changes during development. On P4, microglia (E, green) extend bushy processes, but on P7, microglia (F) present with an ameboid morphology with minimal branching and appear to be engulfing NG2:Tom OPCs (red). Microglia appear less round on P9 (G), with more cellular processes on P11 (H), and show a ramified morphology by P15 (I). Scale bars, 20 μm.

(J) Quantification of microglial engulfment of OPCs was determined by analyzing 3D confocal z stacks using Imaris software from three separate areas of the CC across 3 brain sections (A, white boxes). Engulfed NG2:Tom OPCs were defined as 15% or more of NG2:Tom OPC volume inside of microglia. Contacted NG2:Tom OPCs were defined as less than 15% of NG2:Tom OPC volume within microglia (quantification shown in Figure S1H). The bar graph represents mean ± SEM, n = 3 at P4 and P11, n = 6 at P7, 3 sections, 9 z stacks per animal. Statistical differences were determined using a one-way analysis of variance (ANOVA) with Tukey's multiple comparisons post hoc testing. *p = 0.0431.

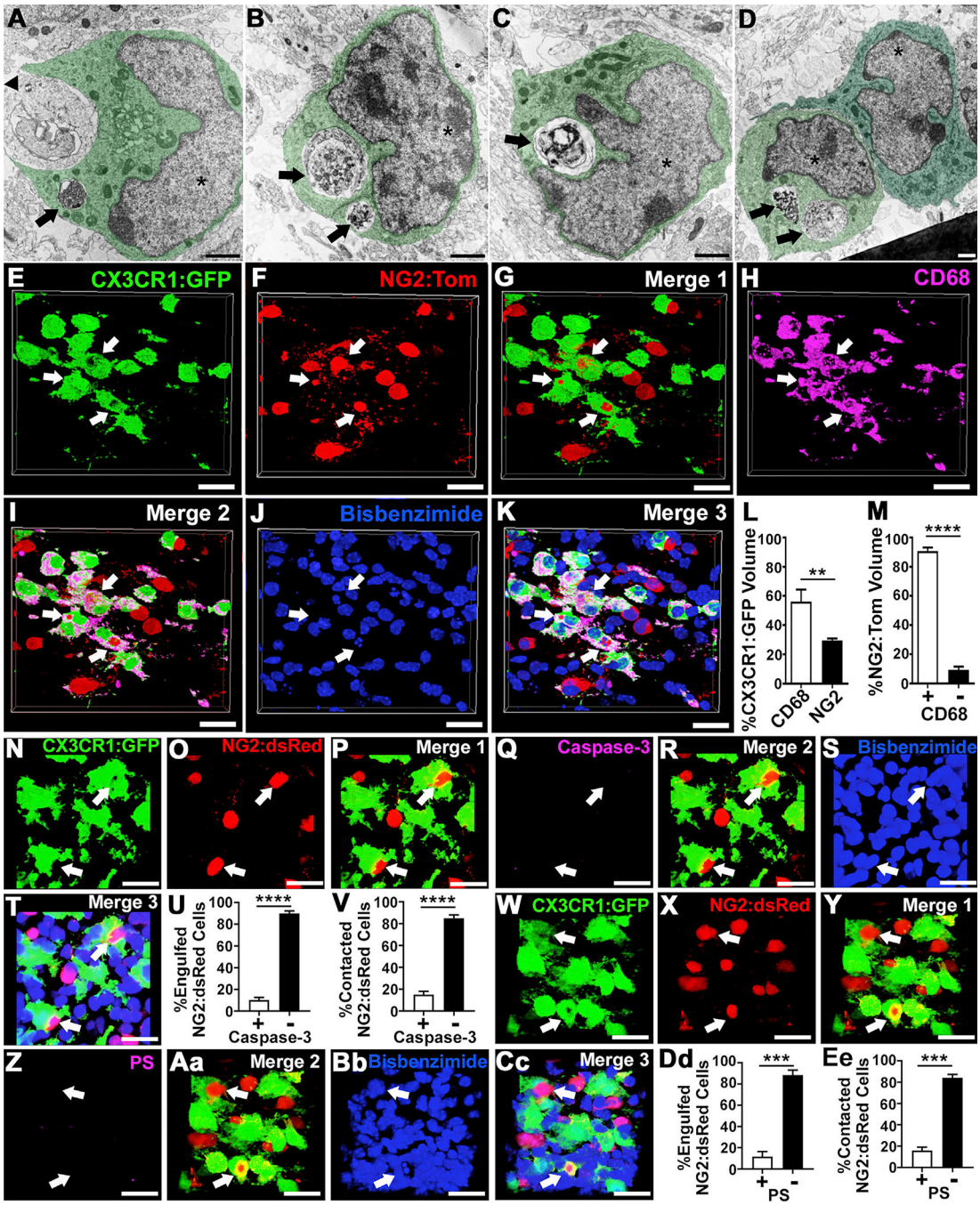

Figure 2. OPCs Engulfed and Phagocytosed by Microglia in the CC on P7 Do Not Express Cell Death Markers

(A–D) EM images from the CC of a P7 mouse show microglia (cytoplasm colorized green, nuclei labeled with asterisks) engulfing cells.

(A) Microglia are observed engulfing a whole cell (arrowhead) with an additional degraded cell (arrow).

(B and C) Microglia are observed phagocytosing multiple cells (arrows).

(D) Microglia are observed interacting with other microglia. Scale bar, 1 μm.

(E–K) Confocal 3D reconstructed image stacks from fixed brains show CX3CR1:GFP microglia (E) engulfing NG2:Tom OPCs (F), which are located within the lysosome of microglia (G, Merge 1), as shown by CD68 staining (H), which colocalizes with engulfed cells (I, Merge 2). Nuclear staining with bisbenzimide (J) colocalized with CX3CR1:GFP;NG2:Tom and CD68 (K, Merge 3) shows nuclei of engulfed OPCs within microglia. Arrows point to engulfed OPCs. Scale bars, 10 μm.

(L) Quantified percent volume of CX3CR1:GFP microglia containing CD68+ lysosomes was 56.07% ± 8.20% and for NG2:Tom cells was 29.48% ± 1.39% (**p = 0.0096).

(M) Quantified percentage of engulfed NG2:Tom OPCs that colocalized with CD68 (denoted +; 90.77% ± 2.32%) or did not colocalize with CD68 (denoted −; 9.23% ± 2.32%). Bar graphs represent ± SEM from 6 animals, 3 sections, 9 z stacks per animal (****p = 0.0001).

(N–V) Confocal 3D reconstruction of fixed brain sections from CX3CR1:GFP (N) NG2:dsRed (O) mice to observe engulfment (P, Merge 1) were stained for caspase-3 (Q), a marker of apoptosis (R, Merge 2) and bisbenzimide nuclear stain (S). Engulfed OPCs (T, Merge 3) were primarily negative for caspase-3 staining (U: Caspase-3+, 10.16% ± 2.33%; caspase-3−, 89.84% ± 2.33%; ****p = 0.0001; V: caspase-3+, 14.96% ± 2.99%; caspase-3−, 85.04% ± 2.99%; ****p = 0.0001).

(W–Ee) Brain sections from CX3CR1:GFP (W) NG2:dsRed (X) mice (Y, Merge 1) were also stained for phosphatidylserine (PS; Z), a marker of cell stress (Aa, Merge 2) and bisbenzimide nuclear stain (Bb). Engulfed OPCs (Cc, Merge 3) were primarily negative for PS staining (Dd: PS+, 11.65% ± 4.77%; PS−, 88.35% ± 4.77%; ***p = 0.0001; Ee: PS+, 15.88% ± 3.24%; PS−, 84.12% ± 3.24%; ***p = 0.0003).

Arrows point to engulfed OPCs. Statistical analyses were determined using two-tailed unpaired t tests. Bar graphs represent mean ± SEM from 6 animals, 3 sections, 3 z stacks per animal in caspase-3 experiments and 3 animals, 3 sections, 3 z stacks per animal in PS experiments for quantification. Scale bars, 20 μm.

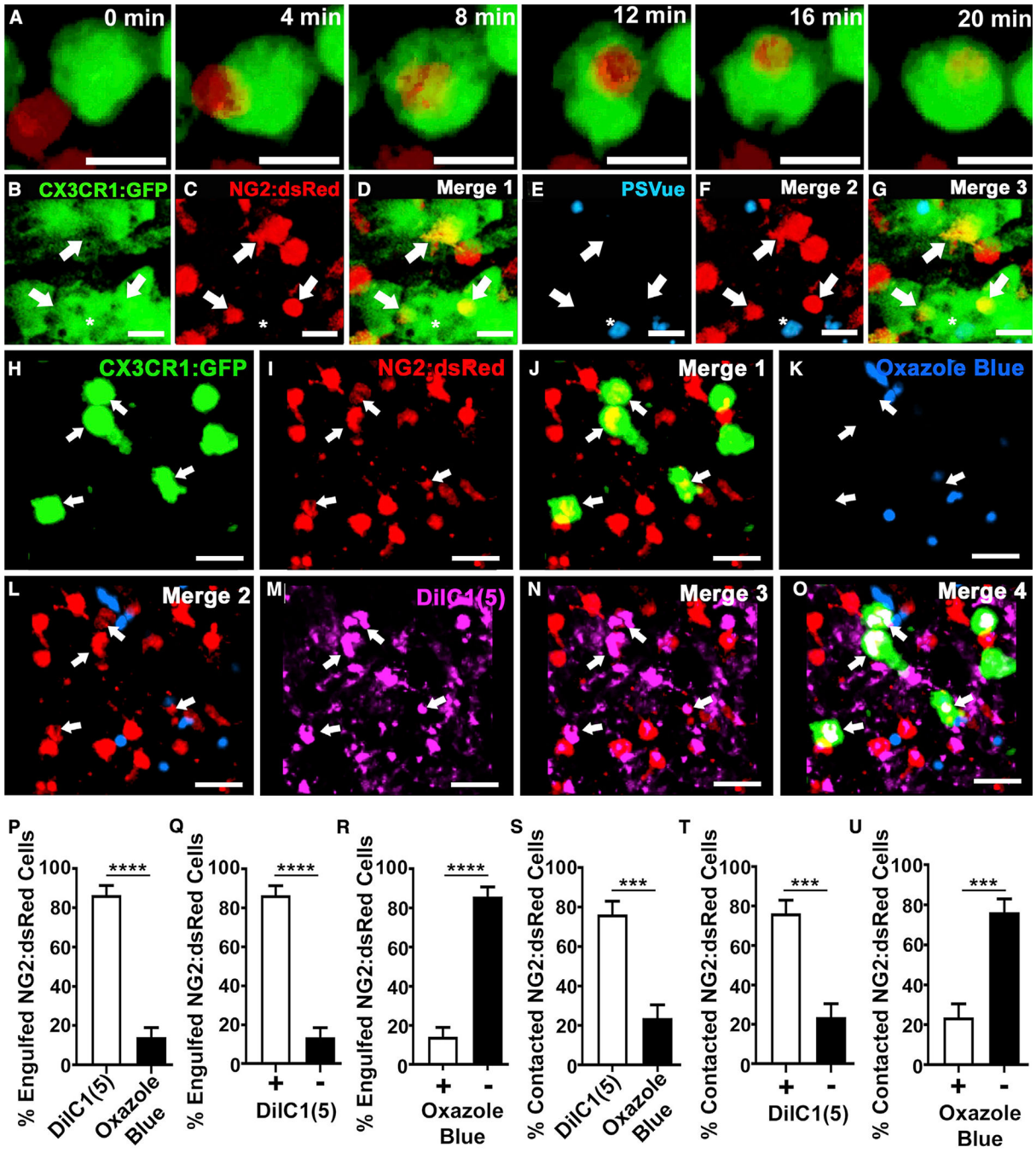

Figure 3. Confocal 3D Imaging of *Ex Vivo* Brain Slices Shows Microglia Phagocytosing Viable OPCs in the CC on P7

(A) 3D confocal reconstructed images from time-lapse microscopy of the CC in a P7 mouse brain expressing CX3CR1:GFP (microglia, green) and NG2:dsRed (OPCs, red). Scale bars, 10 μm. See also Videos S3 and S4.

(B–G) Live imaging experiments show CX3CR1:GFP microglia (B, green) engulfing NG2:dsRed OPCs (C, red) in the P7 CC (D, Merge 1) that are negative for PSVue (E, blue), a dye that labels apoptotic or stressed cells (F, Merge 2). Arrows indicate engulfed NG2:dsRed cells that are negative for PSVue. Asterisks indicate engulfed cells that are

positive for PSVue but negative for NG2:dsRed (G, Merge 3). Scale bars, 10 μm. See also Video S5. Representative of 2 mice, 2 fields of view per section per mouse over 12 h. Quantified videos show only 3 of 32 NG2:dsRed cells expressing PSVue before engulfment and 1 of 32 NG2:dsRed cells expressing PSVue after being engulfed.

(H–O) 3D confocal reconstruction of acute *ex vivo* slices show CX3CR1:GFP microglia (H, green) engulfing NG2:dsRed OPCs (I, red) in the P7 CC (J, Merge 1) that are negative for oxazole blue (K), a marker of cell death (L, Merge 2). DilC1(5) dye (M), a marker of mitochondrial membrane potential (N, Merge 3) was used simultaneously (O, Merge 4), showing that engulfed OPCs are viable. Arrows indicate engulfed NG2:dsRed cells that are negative for oxazole blue but positive for DilC1(5).

(P–R) The majority of engulfed OPCs were viable (P; DilC1(5)+, 86.37 ± 4.94; oxazole blue +, 13.63 ± 4.94; ****p = 0.0001). Engulfed OPCs were primarily positive for DilC1(5) dye (Q; DilC1(5)+, 86.37 ± 4.94; DilC1(5)−, 13.63 ± 4.94; ****p = 0.0001) and negative for oxazole blue dye (R; oxazole blue+, 13.63 ± 4.94; oxazole blue−, 86.37 ± 4.94; ****p = 0.0001).

(S) Contacted OPCs were also viable (DilC1(5)+, 76.29 ± 6.75; oxazole blue+, 23.71 ± 6.75; ***p = 0.0006).

(T and U) Contacted OPCs were predominantly positive for DilC1(5) (T; DilC1(5)+, 76.29 ± 6.75; DilC1(5)−, 23.71 ± 6.75; ***p = 0.0006) and negative for oxazole blue dye (U; oxazole blue+, 23.71 ± 6.75; oxazole blue−, 76.29 ± 6.75; ***p = 0.0006).

Because these images are 3D fields, cells that are farther out of plane may appear to have less expression of the dyes. Therefore, an analysis of dye penetration in all OPCs and microglia is shown in Figures S4J and S4K. Statistical analyses were determined using two-tailed unpaired t tests. Bar graphs represent mean ± SEM from 4 mice, 2 z stacks per mouse. Scale bars, 15 μm.

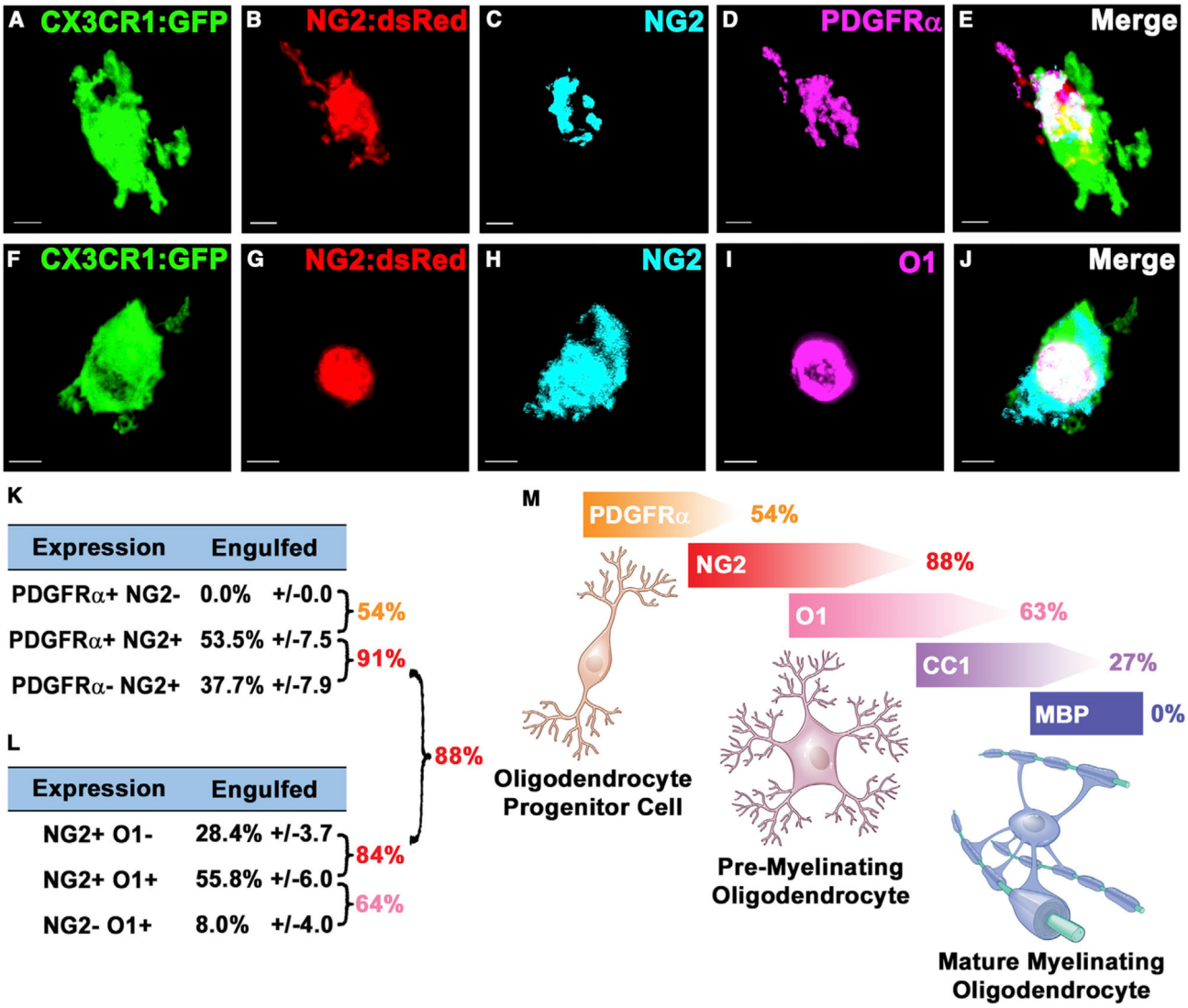

Figure 4. Microglia Engulf NG2+ OPCs that Express Markers of the Pre-myelinating Stage of OL Maturation in the CC on P7

(A–E) Confocal 3D reconstruction of the CC from fixed brain sections shows CX3CR1:GFP microglia (A, green) engulfing NG2:dsRed OPCs (B, red) that express antibodies generated against the early maturation markers NG2 (C, cyan) and PDGFRα (D, pink) (colocalization shown in E, Merge).

(F–J) Evaluation of CX3CR1:GFP microglia (F, green) engulfing NG2:dsRed OPCs (G, red) stained for NG2 (H, cyan) and O1 (I, pink) (colocalization shown in J, Merge). Scale bars, 5 μm.

(K and L) Analysis of PDGFRα/NG2 and NG2/O1 percent colocalization for engulfed NG2:dsRed OPCs (quantification of engulfed and contacted NG2:dsRed OPCs in Figures S5A–S5F; n = 3 mice, 3 z stacks per mouse). Engulfed OPCs were mostly NG2+ ($p = 0.0001$; Figure S5B). Few engulfed OLs expressed CC1 (Figures S5G–S5I), but no engulfed OLs expressed MBP (Figures S6F–S6I).

(M) Summary cartoon shows maturation stages of OLs engulfed by microglia.

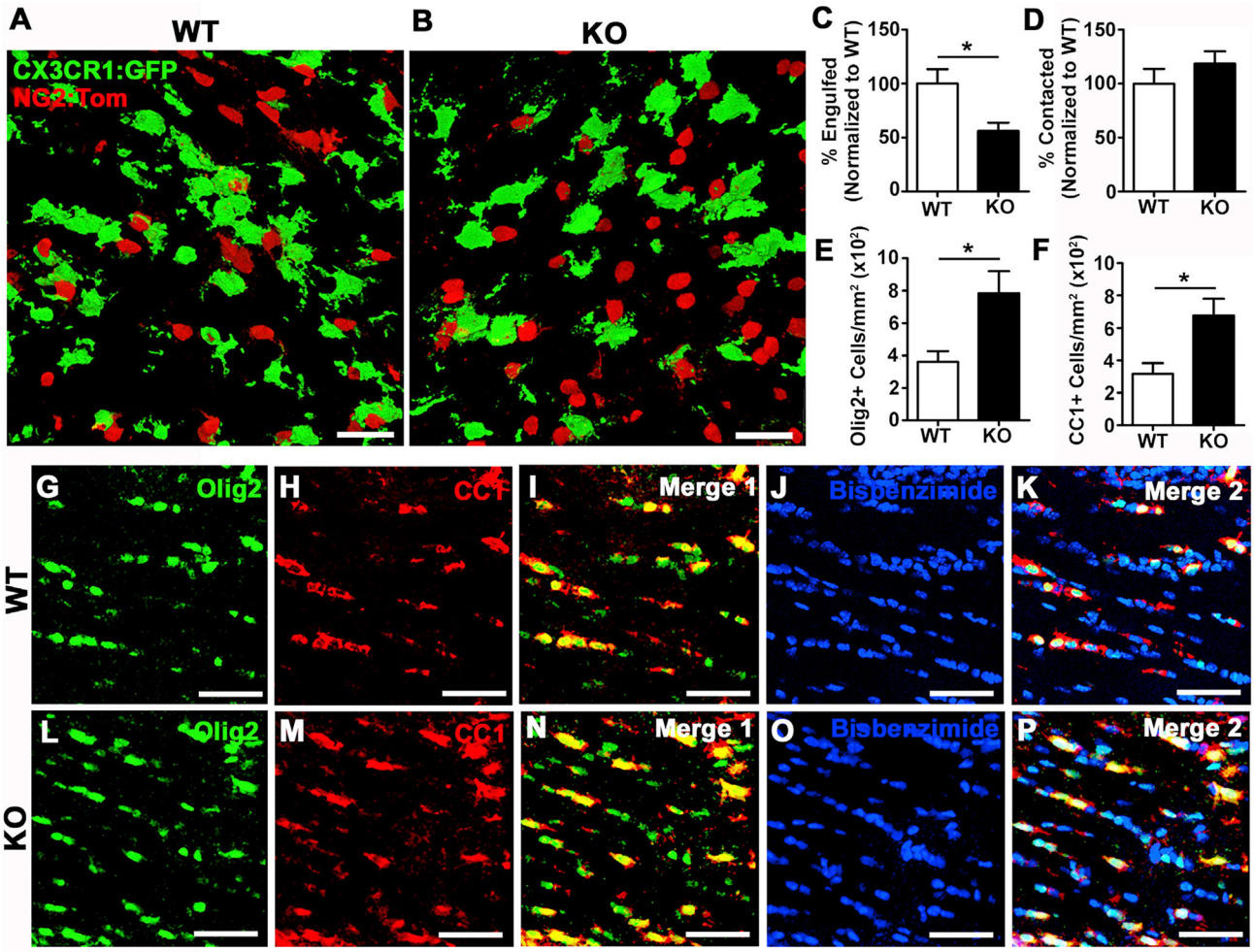

Figure 5. Fractalkine Receptor-Deficient Mice Exhibit a Reduction in Microglial Engulfment of OPCs in the CC on P7 and Increased Numbers of Mature OLs on P30

(A and B) Representative 3D reconstructed images from CX3CR1:GFP (WT, A) and fractalkine receptor-deficient CX3CR1$^{KO/KO}$:GFP mice (KO, B) in the P7 CC from fixed brain sections. Scale bars, 20 μm. Imaris software was used to analyze 3D reconstructed z stacks (depicted in white boxes in Figure 1A) in 9 z stacks per animal from 3 brain sections (WT, n = 6; KO, n = 5).

(C) Engulfment was decreased in KO mice compared with the WT, quantified as 15% or more of NG2:dsRed OPC volume internalized within microglia (*p = 0.0237, two-tailed unpaired t test).

(D) Contacting was not changed in KO compared with WT mice, quantified as less than 15% of NG2:dsRed OPC volume inside microglia (p = 0.3395, two-tailed unpaired t test).

(E and F) In the P30 CC, cell counts of Olig2+ (E) and CC1+ cells (F) were increased in KO compared with WT mice. *p = 0.0482 and *p = 0.0428, respectively; two-tailed unpaired t tests (n = 3 mice per group, 6 fields per animal from 3 brain sections).

(L–P) Representative images show staining in WT (G–K) and KO CC (L–P), with Olig2 stained in green (G and L), CC1 stained in red (H and M), a merge of the two colors (Merge

1, I and N), bisbenzimide in blue (J and O), and a merge of all three colors (Merge 2, K and P).

Scale bars, 25 μm. Bar graphs represent mean ± SEM.

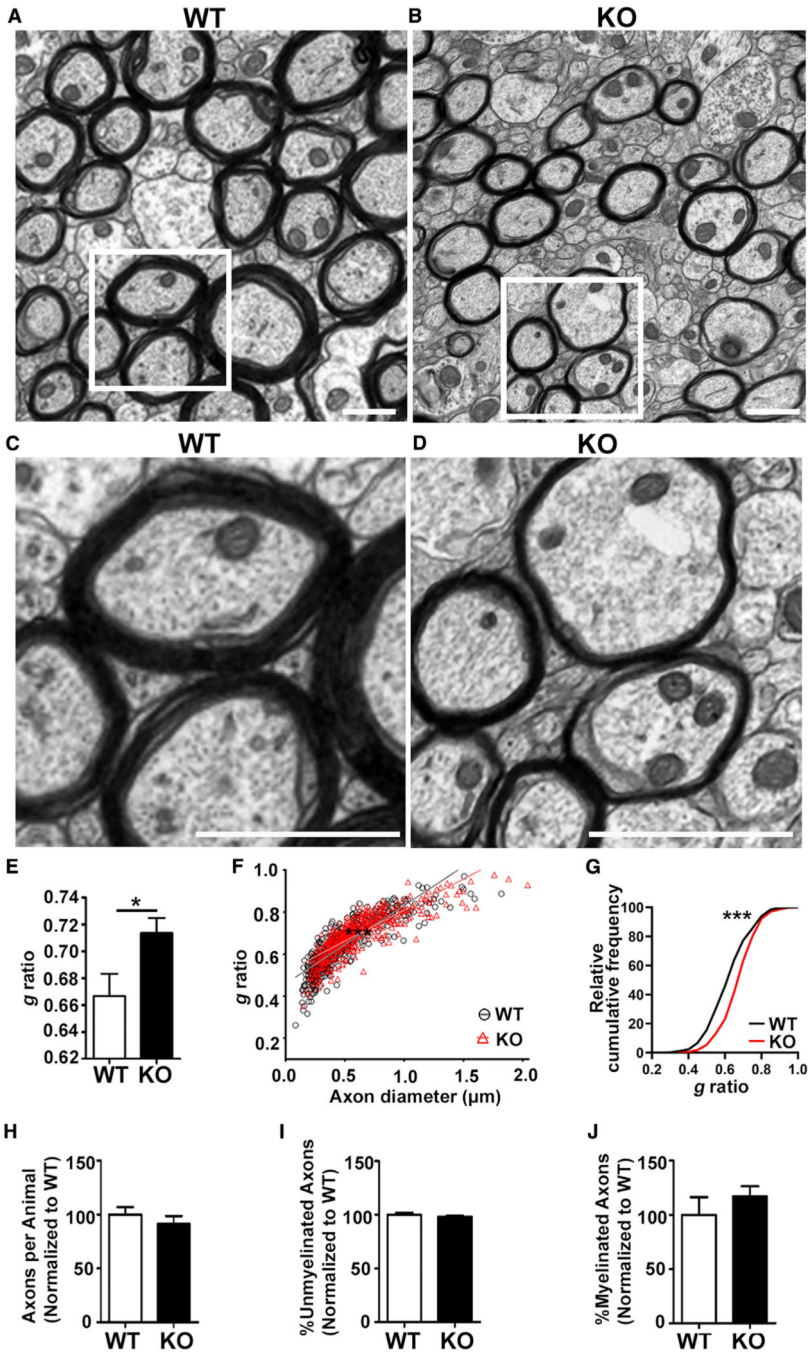

Figure 6. Reduced Engulfment of OPCs by Fractalkine Receptor KO Leads to Impaired Myelin Formation on P30 in the CC

(A and B) Representative ultrastructural images from CX3CR1:GFP (WT, A) and fractalkine receptor-deficient CX3CR1$^{KO/KO}$:GFP mice (KO, B) in the P30 CC. Scale bars, 2 μm.

(C and D) Magnified images show a decrease in myelin thickness in KO mice (C) compared with the WT (D). Scale bars, 1 μm.

(E) A decrease in myelin thickness (increased g ratio, axon diameter divided by axon plus myelin diameter) was found in KO versus WT mice; ***p = 0.0001, two-tailed unpaired t test (n = 6 mice per group, 10 fields per mouse).
(F) Scatterplot displaying g ratios of individual myelinated axons as a function of axon diameter; analysis of covariance (ANCOVA) shows a statistically significant difference (***p = 0.0001) between WT and KO.
(G) Relative cumulative frequency distributions show a statistically significant shift in g ratio (G); ***p = 0.0001 Kolmogorov-Smirnov test.
(H and I) No differences were observed in the number of axons per animal (H) or percentage of unmyelinated (I) or myelinated (J) axons in KO mice compared with the WT.
Bar graphs represent mean ± SEM.

KEY RESOURCE TABLE

REAGENT or RESOURCE	SOURCE	IDENTIFIER
Antibodies		
rabbit anti-Iba-1 (1:750)	Wako	Cat# 019-19741; RRID: AB_839504
rabbit anti-caspase-3 (1:200)	Abcam	Cat# ab32042; RRID: AB_725947
mouse anti-phosphatidylserine (1:200 without triton)	Millipore	Cat# 05-719; RRID: AB_309933
mouse anti-CD68 (1:200)	Biorad	Cat# mca1957 ga; RRID: AB_324217
rat anti-PDGFRα (1:400)	BD Bioscience	Cat# 558774; RRID: AB_397117
rabbit anti-NG2 (1:200 free-floating)	Millipore	Cat# ab5320; RRID: AB_91789
mouse anti-O1 (1:100 free-floating without triton)	Millipore	Cat# mab344; RRID: AB_11211821
mouse anti-CC1 (1:100)	Millipore	Cat# OP80; RRID: AB_2057371
rat anti-MBP (1:400)	Abcam	Cat# ab7349; RRID: AB_305869
and rabbit anti-Olig2 (1:200)	Millipore	Cat# ab9610; RRID: AB_570666
Alexa Fluor 488 goat anti-rabbit IgG (1:1000)	Invitrogen	Cat# A11034; RRID: AB_2576217
Alexa Fluor 647 goat anti-rabbit IgG (1:1000)	Invitrogen	Cat# A21245; RRID: AB_2535813
Alexa Fluor 647 goat anti-mouse IgG (1:1000)	Invitrogen	Cat# A21235; RRID: AB_2535804
Alexa Flour 647 goat anti-rat (1:1000)	Invitrogen	Cat# A21247; RRID: AB_141778
Biotinylated goat anti-rabbit IgG (1:200)	Vector Labs	Cat# BA-1000; RRID: AB_2313606
Alexa Fluor 647 goat anti-mouse IgM (1:500)	Abcam	Cat# ab150123
Chemicals, Peptides, and Recombinant Proteins		
405 conjugated streptavidin DyLight (1:1000)	Thermo Scientific	Cat# 21831
Tamoxifen	Sigma-Aldrich	Cat# T5648
Fluoromount-G	Southern Biotech	Cat# 0100-01
Bisbenzimide (1:1000)	Invitrogen	Cat# H3569; RRID: AB_2651133
PSVue dye 643	Molecular Targeting Technologies	Cat# PSVue-643
Oxazole blue 455	Biotium	Cat# 40091
DilC1(5) 658	Biotium	Cat# 70015
Experimental Models: Organisms/Strains		
B6.Cg-Tg(Cspg4-cre/Esr1*)BAkik/J (NG2-CreER™)	Jackson Laboratory	Cat# Jax 008538; RRID: IMSR_JAX:008538
B6.Cg-Gt(ROSA)26Sortm14(CAG-tdTomato)Hze/J	Jackson Laboratory	Cat# Jax 007914; RRID:IMSR_JAX:007914
Tg(Cspg4-DsRed.T1)1Akik/J (NG2DsRedBAC)	Jackson Laboratory	Cat# Jax 008241; RRID: IMSR_JAX:008241
B6.129(Cg)-Ccr2tm2.1Ifc/J ($Ccr2^{RFP}$)	Jackson Laboratory	Cat# Jax 017586; RRID: IMSR_JAX:017586
B6.129P2(Cg)-Cx3cr1tm1Litt/J (CX3CR1-GFP)	Jackson Laboratory	Cat# Jax 005582; RRID: IMSR_JAX:005582
Software and Algorithms		
Imaris	Bitplane	https://imaris.oxinst.com/
FIJI	ImageJ	https://imagej.net/Fiji
NIS-Elements	Nikon	https://www.microscope.healthcare.nikon.com/products/software/nis-elements
Prism	GraphPad	https://www.graphpad.com/scientific-software/prism/

REAGENT or RESOURCE	SOURCE	IDENTIFIER
SPSS	IBM	https://www.ibm.com/analytics/spss-statistics-software